Cell-surface SLC nucleoside transporters and purine levels modulate BRD4-dependent chromatin states

Kai-Chun Li[1], Enrico Girardi[1], Felix Kartnig[1], Sarah Grosche[1], Tea Pemovska[1], Johannes W. Bigenzahn[1,2], Ulrich Goldmann[1], Vitaly Sedlyarov[1], Ariel Bensimon[1], Sandra Schick[1], Jung-Ming G. Lin[1], Bettina Gürtl[1], Daniela Reil[1], Kristaps Klavins[1], Stefan Kubicek[1,3], Sara Sdelci[4], Giulio Superti-Furga[1,5]

[1]CeMM, Research Center for Molecular Medicine of the Austrian Academy of Sciences, Vienna, Austria
[2]Department of Laboratory Medicine, Medical University of Vienna, Vienna, Austria
[3]Christian Doppler Laboratory for Chemical Epigenetics and Antiinfectives, CeMM Research Center for Molecular Medicine of the Austrian Academy of Sciences, Vienna, Austria
[4]Centre for Genomic Regulation, The Barcelona Institute of Science and Technology, Barcelona, Spain
[5]Center for Physiology and Pharmacology, Medical University of Vienna, Vienna, Austria

Correspondence to:
Giulio Superti-Furga
CeMM Research Center for Molecular Medicine of the Austrian Academy of Sciences
Lazarettgasse 14, AKH BT25.3
1090 Vienna, Austria
E-mail: gsuperti@cemm.oeaw.ac.at
Telephone: +43 1 40160 70 001

Abstract

Metabolism negotiates cell-endogenous requirements of energy, nutrients and building blocks with the immediate environment to enable various processes, including growth and differentiation. While there is an increasing number of examples of crosstalk between metabolism and chromatin, few involve uptake of exogenous metabolites. Solute carriers (SLCs) represent the largest group of transporters in the human genome and are responsible for the transport of a wide variety of substrates, including nutrients and metabolites. We aimed at investigating the possible involvement of SLC-mediated solutes uptake and cellular metabolism in regulating cellular epigenetic states. Here, we perform a CRISPR/Cas9 transporter-focused genetic screen and a metabolic compound library screen for the regulation of BRD4-dependent chromatin states in human myeloid leukemia cells. Intersection of the two orthogonal approaches reveal that loss of transporters involved with purine transport or inhibition of de novo purine synthesis lead to dysfunction of BRD4-dependent transcriptional regulation. Through mechanistic characterization of the metabolic circuitry, we elucidate the convergence of SLC-mediated purine uptake and *de novo* purine synthesis on BRD4 chromatin occupancy. Moreover, adenine-related nucleotides supplementation effectively restores BRD4 functionality upon purine impairment. Our study highlights the specific role of purine/adenine metabolism in modulating BRD4-dependent epigenetic states.

Introduction

Chromatin remodeling and the associated epigenetic events resulting in changes in gene expression are fundamental mechanisms regulating cellular states and normal physiology[1]. Coordinated dynamics of chromatin regulation is essential for cells to adapt to external challenges, while epigenetic aberrations contribute to diverse aspects of pathological conditions such as cancer[2,3]. Deciphering the various mechanisms by which environmental clues give rise to changes in chromatin regulation will help to elucidate how cellular states are achieved and enable identifying avenues of therapeutic homeostasis restauration.

Accumulating evidence has highlighted that epigenetic dynamics are directly driven by cellular metabolic states, as shown by the reliance of epigenetic enzymes on intermediary metabolites acting as substrates or cofactors, such as acetyl-CoA or S-adenosylmethionine (SAM)[4-5]. Metabolism is comprised of a complex network of synthesis and degradation reactions, transforming nutrients derived from the extracellular environment into building blocks and energy equivalents necessary for cell growth, division and waste removal. Uptake of nutrients and removal of catabolites at cellular membranes are therefore key determinants of metabolic fluxes. Solute carriers (SLCs) represent the largest group of transmembrane transporters in the human genome, comprising more than 400 genes in 65 subfamilies[6,7]. SLCs are responsible for the transport of a large variety of molecular classes, including amino acids, carbohydrates, metals, ions and nucleosides[6]. SLCs are therefore central to controlling the metabolic state of cells by determining nutrient availability[8] or by acting as transceptors[9]. Roughly two-thirds of SLCs locate at the plasma membrane controlling the cellular uptake and release of substrates across the membrane[7, 10]. Despite the significant role of SLCs in driving metabolic dynamics, our understanding of how specific SLCs can initiate metabolic changes that influence the state of chromatin is still sporadic.

BRD4, a histone acetylation reader important in epigenetic and transcriptional regulation, is receiving considerable attention as a therapeutic target in the context of cancer due to its dominant role in regulating the transcription of oncogenic driver genes, particularly *MYC*, and associated enhancers[11-12]. To explore factors regulating BRD4 functionality, we previously established the BRD4 inhibition-based cellular reporter system REDS (Reporter for Epigenetic Drug Screening) in the human near-haploid chronic myeloid leukemia (CML) cell line KBM-7[13]. REDS is defined by a single red fluorescent protein (RFP) integration at a genomic locus that specifically becomes actively transcribed once BRD4 is inhibited, therefore responding to BRD4 inhibition by the expression of RFP (Extended Data Fig. 1a)[13,14]. Given a robust fluorescence-based readout of BRD4-related chromatin states, REDS is suitable for both, genetic and pharmacological screens. Utilizing a gene-trap mutagenesis-based genetic screen on REDS, we recently identified MTHFD1, an enzyme involved in folate metabolism, as a BRD4 interactor on chromatin that is required for BRD4 to exert its regulatory function on transcription[14]. Following the implication that the metabolic activity of the cell could contribute to BRD4-chromatin dynamics, we systematically investigated the involvement of SLC transporters in the axis linking nutrient availability, metabolism and BRD4 regulation.

Results

SLC-mediated purine uptake regulates activity of BRD4

By taking advantage of the REDS approach, we performed a fluorescence-activated cell sorting (FACS)-based genetic loss-of-function screen using an SLC-focused CRISPR/Cas9 library targeting 394 human SLC genes and pseudogenes[15] in three independently derived REDS clones (REDS1, REDS15 and REDS17). REDS1 is characterized by a single RFP insertion in the first intron of *CDKAL1*[14]. REDS15 and REDS17 have an RFP integration at the chromosomal 12q24.33 locus, 410 and 672 bp upstream of *STX2*, respectively (Extended Data Fig. 1b), similarly to the previously described REDS3 clone[13]. The three REDS clones were individually transduced with a pooled SLC knockout library and sorted to collect the highest 0.5 % RFP-expressing cells (Fig. 1a). Comparing the difference in sgRNA enrichment between sorted and unsorted populations, we identified SLCs for which depletion mimicked BRD4 functional inhibition, turning the cells RFP-positive (Fig. 1b). We validated the findings by examining the RFP expression level in REDS1 and REDS15 clones following the depletion of the candidate SLC genes 12 days after sgRNA transduction. The results confirmed that *SLC28A3*, *SLC29A4*, *SLC35F5* and *SLC6A8* knockout led to a prominent induction of RFP expression (Fig. 1c). SLC28A3 and SLC29A4 are members of nucleoside transporter families responsible for nucleosides transport across the plasma membrane[16-18]. SLC35F5 belongs to the SLC35 family transporting nucleotide-sugars across biological membranes[19]. Although the substrates of SLC35F5 are poorly characterized, members of the nucleotide-sugar transporters family have been reported to interact with nucleoside monophosphates[20], and SLC35F5 was shown to affect cellular chemosensitivity to nucleoside analogues[21], suggesting a potential role in nucleosides transport and metabolism. Given the possible functional overlap between these three SLCs, we generated dual and triple SLC knockouts in REDS15 cells (Extended Data Fig. 2). 12 days after sgRNA transduction, a more pronounced RFP expression was observed in the triple SLC knockout (SLC TKO) cells compared to the single or dual knockout cells (Fig. 1d).

These data suggested that the role of the SLCs under investigation was to transport environmental solutes, potentially nucleosides, that inside the cell were required to maintain BRD4 functionality. To test this hypothesis, REDS clones were cultured in growth medium with either normal or dialyzed serum deprived of small molecules (e.g., nucleosides). We observed a gradual increase in RFP expression in both clones when supplied with dialyzed serum, suggesting that soluble components lost by dialysis were required for optimal BRD4 activity (Extended Data Fig. 3a). We further examined whether exogenous nucleosides supplementation could rescue the observed BRD4 inhibition phenotype, in order to evaluate the involvement of nucleosides transport in BRD4 functionality. Purine nucleosides supplementation reduced RFP expression in REDS clones growing in dialyzed serum as well as with selected SLC knockouts, whereas pyrimidine supplementation had no impact on RFP expression (Fig. 1e, Extended Data Fig. 3b,), implicating a purine-specific effect on BRD4 regulation. The decrease of RFP expression was less pronounced in REDS15 cells with triple SLC knockout compared to the single knockout upon purine supplementation (Fig. 1e), most probably due to the additional impairment in nucleoside import upon the loss of multiple transporters. Together, these data suggested that exogenously added purines result in changes in BRD4 functionality in a manner dependent on the expression of specific SLC transporters.

To corroborate the involvement of these SLCs in BRD4 regulation, we overexpressed sgRNA-resistant SLC28A3 or SLC29A4 in the respective SLC knockout REDS15 cells. Expression of each of the wild-type (WT) transporters rescued the phenotype and effectively abrogated RFP expression. Transporter activity defective mutants described previously[22,23] failed to reduce RFP expression, indicating that the nucleoside transport function is crucial for BRD4 functionality (Fig. 1f, g). Although we failed to overexpress SLC35F5 in REDS cells, the detection of enhanced RFP expression in the triple SLC knockout cells compared to SLC28A3/SLC29A4 dual knockout cells (Fig. 1d) indicated a non-redundant role for SLC35F5 in BRD4 regulation. These observations supported a functional link between SLC-mediated extracellular purine uptake and BRD4.

Inhibition of *de novo* purine synthesis inactivates BRD4

If intracellular purine concentrations were indeed important for the regulation of BRD4, other perturbations that reduce the purine pools should mimic the loss of transporter function. As an orthogonal approach, we tested whether compounds with metabolic activities may lead to BRD4 inhibition. To scout for metabolic compounds able to induce RFP expression, we established an image-based screen in REDS clones, using KBM-7 WT cells as negative control (Fig. 2a). This custom-made library contains 243 compounds broadly targeting eight metabolic pathways/processes, including nucleotide metabolism (Extended Data Fig. 4a, Supplementary Table 1). We observed increased RFP expression upon the treatment of the potent bromodomain and extra terminal protein inhibitor (BETi) CPI-0610 and the purine analog 6-mercaptopurine (6-MP) (Fig. 2b, Extended Data Fig. 4b), as well as the auto-fluorescent compound NSC-95397. Although 6-MP treatment was not as efficient as direct inhibition of BRD4 by (+)-JQ1 or CPI-0610 in inducing RFP expression, the effect was consistent across REDS clones and the different time points. 6-MP interferes with purine metabolism by inhibiting amidophosphoribosyltransferase (*PPAT*), the first enzyme gate-keeping the entire *de novo* purine synthesis pathway. Azathioprine is a pro-drug that is non-enzymatically converted to 6-MP. 6-MP is then processed either into its active derivative 6-thioinosine monophosphate (TIMP) which inhibits *de novo* purine synthesis, or into the inactive derivate 6-thiouric acid (6-TU) (Fig. 2c)[24]. To understand whether the increased RFP expression following 6-MP treatment was due to direct impact on *de novo* purine synthesis, we treated REDS clones with 6-MP related compounds. Azathioprine and TIMP, but not 6-TU, induced RFP expression in a dose-dependent manner (Fig. 2d, Extended Data Fig. 4c). Chemically inhibiting the second enzyme of *de novo* purine synthesis, glycinamide ribonucleotide transformylase (*GART*), with pelitrexol or lometrexol, also triggered RFP expression (Extended Data Fig. 4d), confirming a central role of this pathway in BRD4 regulation. In contrast, none of the pyrimidine metabolism inhibitors from the metabolic compound library induced RFP expression (Fig. 2b, Supplementary Table 1). To confirm this result, we treated REDS clones with three of the pyrimidine metabolism inhibitors selected from the library, teriflunomide, brequinar and 5-FU, and examined the RFP expression. After 72 h treatment, no significant RFP induction was observed (Extended Data Fig. 4e), ruling out the involvement of pyrimidine metabolism in regulating BRD4 functionality. Interestingly, treatment with arsenic trioxide, which blocks MTHFD1 nuclear localization[25], induced RFP expression in REDS15 and REDS17 clones (Fig. 2b), consistent with our previous

finding that blocking the function of nuclear MTHFD1 leads to BRD4 inhibition[14]. Together with the results observed in the SLC loss-of-function screen, our data strongly suggested that intracellular purine levels were involved in BRD4 functional control. We therefore challenged this hypothesis by systematically assessing the BRD4-inhibition effects by knocking out seventeen purine metabolism genes individually in REDS15 cells, of which ten involved in *de novo* purine synthesis, five in degradation and two in salvage pathway (Extended Data Fig. 4f)[26] and monitored RFP expression. Remarkably, nine out of ten *de novo* purine synthesis genes functionally assessed by knockout led to increased RFP expression whereas cells with deficient purine degradation or salvage pathway did not show significant induction of RFP signal (Fig. 2e), demonstrating a specific involvement of *de novo* purine synthesis in BRD4 regulation.

Purine effects BRD4-mediated transcriptional regulation

To investigate whether the above observed effects were due to changes in intracellular purine pools, we performed mass spectrometry-based targeted metabolomics to monitor the levels of a set of 40 metabolites in REDS15 cells bearing triple SLC knockout and in cells treated with 6-MP or (+)-JQ1. Of all classes of metabolites monitored, nucleotides/nucleosides were most affected upon (+)-JQ1 treatment. In addition, 6-MP treatment as well as the SLC knockout strongly reduced nucleotide/nucleoside levels, with a more pronounced effect on purines and their precursors, showing a strong correlation with the changes observed upon (+)-JQ1 treatment (Fig. 3a, Supplementary Table 2).

Binding of BRD4 to acetylated chromatin activates the cellular transcriptional machinery. Inhibition of BRD4 leads to its widespread eviction from chromatin, thereby causing transcriptional inactivation[27]. Having previously characterized the fidelity of the REDS in reflecting BRD4 function, we therefore sought to investigate whether purine metabolism affects BRD4 directly by investigating its subcellular compartment and chromatin-binding activity. By performing chromatin-nucleoplasm fractionation, we found that REDS15 cells treated with *de novo* purine synthesis inhibitors or bearing triple SLC knockout displayed decreased levels of BRD4 on chromatin but increased amounts of BRD4 in the nucleoplasm compared to their respective controls (Fig. 3b, Extended Data Fig. 5a). Neither BRD4 protein, nor its related acetylation marker on histone 3 lysine 27 (H3K27), nor pan acetylation level on histone 3 were reduced (Extended Data Fig. 5b, c), suggesting the disassociation of BRD4 from chromatin was not due to decreasing histone acetylation abundance upon impaired purine metabolism. Consistently, we observed a global loss of BRD4-genome occupancy in REDS15 cells with above treatments, mimicking the consequence of (+)-JQ1 treatment performing BRD4 chromatin immunoprecipitation-sequencing (ChIP-seq) (Fig. 3c, d, Extended Data Fig. 6b, c). Specific analysis on the loci of two important BRD4 target genes in leukemia, *MYC* and *BCL-2*, revealed that the above treatments resulted in a reduction of BRD4 occupancy on their promoter regions (Fig. 3e, Extended Data Fig. 6d). These findings demonstrated the specificity of intracellular purine levels on regulating BRD4-chromatin occupancy.

Next, we investigated whether the changes in BRD4-chromatin binding observed when dampening purine levels may result in transcriptional changes similar to direct BRD4 inhibition. We performed gene expression profiling following treatment with 6-MP or (+)-JQ1 and in triple SLC knockout cells. A strong correlation between all the treatments at the transcriptional level was observed, suggesting the convergence on

a related mechanism (Extended Data Fig. 7a, b). Gene set enrichment analysis (GSEA) of the downregulated genes further revealed a significant enrichment in MYC- and E2F-dependent transcriptional signatures, both of which are BRD4 target genes (Extended Data Fig. 7c, d)[28]. Real-time PCR analysis confirmed that 6-MP treatment or triple SLC knockout led to a reduction of *MYC* transcripts (Extended Data Fig. 7e). Of note, we observed a similar downregulation of *de novo* purine synthesis genes following acute treatment with 6-MP and (+)-JQ1, but not upon SLC knockout (Extended Data Fig. 7f). The latter observation may be due to a feedback mechanism while cells were deficient in importing nucleosides, may activate compensatory pathways to overcome this metabolic bottleneck. Altogether, these data indicated that imbalance in intracellular purine pools, resulting from either inhibiting purine uptake or *de novo* purine synthesis, leads to impaired BRD4-mediated transcriptional regulation.

Purine uptake and synthesis converge on BRD4 regulation

Purine uptake from the environment and *de novo* purine synthesis both impinge on BRD4 function. We next investigated how these two pathways may converge. If BRD4 inhibition and cell viability manifested by defective *de novo* purine synthesis was connected to the reduction of intracellular purine pools, increase in purine uptake from the environment may rescue the phenotype. As expected, depleting the *PPAT* gene resulted in a robust induction of RFP expression and reduction in cell viability (Fig. 4a, b). Overexpression of SLC28A3 or SLC29A4, as well as extracellular purine supplementation, attenuated RFP expression and restored cell fitness (Fig. 4a-d), suggesting a dependence on available purine as a common BRD4 regulatory mechanism and a compensatory metabolic equilibrium between purine uptake and *de novo* purine synthesis. We next explored the relative contribution of both pathways to intracellular purine pools. To address this, we performed stable isotope tracing experiments coupled with mass spectrometry by supplementing the cell culture medium with +1 ^{13}C-adenine, which could be directly transported by nucleoside transporters, and +3 $^{13}C_2$,^{15}N-glycine, which provided the backbone for purine scaffold in *de novo* synthesis. Measurement of the pattern of resultant labeled AMP levels in hydrolyzed nucleic acid samples, coming either directly from labeled adenine or glycine was used to assess the relative contribution of each pathway. REDS15 cells bearing triple SLC knockout, had decreased level of +1 and increased level of +3 labeled-AMP abundance compared to the vehicle group. In contrast, cells treated with 6-MP displayed a decreased level of +3 and increased level of +1 labeled-AMP (Fig. 4e). These findings revealed that cells with inhibited purine uptake rely more on *de novo* purine synthesis to maintain intracellular purine levels, while cells with impaired *de novo* purine synthesis rely on increased purine uptake from the environment. Simultaneous impairment of both pathways additively led to BRD4 inhibition and impaired cell viability (Fig. 4f, g), once again indicating that SLC-mediated purine uptake and *de novo* purine synthesis converge on BRD4 regulation.

SLC functional redundancy can restore BRD4 activity

While monitoring REDS cells with SLC knockout, we noticed an unexpected loss of the BRD4 inhibition phenotype, reflected by the loss of RFP expression, around day 23 post sgRNA transduction (Extended Data Fig. 8a). No difference was observed in sgRNA editing efficiencies compared to those observed at day 12,

excluding the possibility of a selection of non-edited cells over time (Extended Data Fig. 8b). Neither significant metabolic changes, nor impairment of BRD4 chromatin-nucleoplasm distribution were observed at day 23 (Supplementary Table 2, Extended Data Fig. 8c, d). In line with the fact that triple SLC knockout cells at day 12 did not show significant expressional changes of *de novo* purine synthesis genes (Extended Data Fig. 7f), we speculated that knocking out several SLCs with related transport profiles may activate metabolic compensatory route(s) to rescue BRD4 inhibition conferred by the lack of purine uptake, resulting in a full recovery around day 23.

Given the convergence of purine uptake and *de novo* purine synthesis, we explored whether the dynamic balance between these two pathways is associated with the recovery of BRD4 function. If *de novo* purine synthesis addition was the compensatory route to reactivate BRD4 in triple SLC knockout cells on day 23, inhibiting this pathway should have a more pronounced effect on growth inhibition and RFP induction. To test this hypothesis, we examined the cell viability with *de novo* purine synthesis inhibition by lometrexol treatment. The REDS15 triple SLC knockout day 12 cells were more sensitive to lometrexol treatment compared to the sg*Ren* cells due to the combinatorial inhibition of purine uptake and *de novo* purine synthesis (Extended Data Fig. 8e), consistent with our previous findings (Fig. 4g). However, this differential growth inhibition effect was not observed at day 23 (Extended Data Fig. 8e). Additionally, lometrexol treatment was unable to boost RFP expression in triple SLC knockout day 23 cells (Extended Data Fig. 8f), suggesting that other factors beyond *de novo* purine synthesis were required for triple SLC knockout day 23 cells to re-balance the intracellular purine levels, therefore regaining full BRD4 functionality.

Functional redundancy within the SLC superfamily has been reported for several metabolite classes[6,15]. Inhibition of one SLC often results in expressional changes or a pharmacokinetic alteration of other SLCs[29], suggesting a presence of an integrated transporter functional network preserving metabolic homeostasis. In line with the presence of the overlapping SLC substrates preferences[29], we hypothesized that the loss of certain SLCs may trigger metabolic compensations via SLCs crosstalk. In this respect, we therefore investigated whether any SLC compensatory mechanism could take place, thereby restoring BRD4 activity in triple SLC knockout cells on day 23. We compared the transcriptional profiles of SLC nucleoside transporter and nucleotide-sugar transporter family genes to investigate whether purine metabolism recovery on day 23 was associated with the transcriptional upregulation of any of these SLCs involved in uptake of the purine-related metabolites. No significant upregulation of the listed SLCs was observed (Extended Data Fig. 8g), suggesting the compensatory response was not related to the transcriptional changes of these SLCs. However, by performing the stable isotope tracing experiment described above, we found that +1 labeled-AMP, reflecting purine uptake from the environment, was inhibited on day 12 but later recovered on day 23. On the other hand, +3 labeled-AMP, coming from *de novo* purine synthesis, was originally upregulated on day 12 but further decreased on day 23 (Extended Data Fig. 8h), indicating that the recovery of purine metabolism was presumably achieved by restoration of purine uptake. While the metabolic compensatory mechanism in triple SLC knockout cells on day 23 was not entirely elucidated here, our data pointed towards an enhanced purine uptake capability, likely related to the high degree of functional redundancy observed among cellular transporters.

Inhibition of purine metabolism sensitizes cells to BRD4 inhibitors

As impaired purine metabolism led to BRD4 dysfunction, we postulated that this might sensitize cells to BRD4 inhibition. Upon (+)-JQ1 treatment, a considerable induction of RFP expression was detected in REDS cells bearing triple SLC knockout compared to control cells (Fig. 4h). A similar synergistic effect was observed when combining treatment with 6-MP and (+)-JQ1, compared to the treatment with the individual compounds (Fig. 4i). To further evaluate whether this synergy affected cellular viability, we combined 6-MP treatment with CPI-0610 in three BETi insensitive leukemia cell lines, Jurkat E6.1, Raji and K562 (Genomics of Drug Sensitivity in Cancer database). In all three cell lines, a considerable reduction on cell viability was observed, contrary to the respective single treatments (Extended Data Fig. 9a, b). To quantify the drug interaction effects of 6-MP and CPI-0610, we calculated the combination drug index (CDI), whereby scores <1, =1 or >1, indicate synergistic, additive or antagonistic effects, respectively[30,31]. The CDI was calculated as 0.39 in Jurkat E6.1, 0.35 in Raji and 0.24 in K562 cells, indicative of substantial synergy, highlighting a pharmacologically actionable axis connecting purine metabolism and BRD4-dependent chromatin states.

Adenine-dependent metabolic regulation mediates chromatin binding

To gain insight into the purine specific regulation on BRD4, we evaluated the rescuing effect of individual purine-related metabolites on BRD4 functionality in cells with impaired purine metabolism. A dose-dependent decrease on RFP expression was found in REDS cells bearing triple SLC knockout, with 6-MP treatment as well as with nucleoside transporter SLC29A4 inhibition by TC-T 6000[32] treatment while supplemented with AICAR, IMP, AMP, ADP, ATP, adenine, adenosine or hypoxanthine (Fig. 5a, b, Extended Data Fig. 10a). Strikingly, these metabolites contain either an adenine base or are connected to adenine catabolism. None of the guanine-related nucleotides was sufficient to rescue BRD4 functionality upon purine metabolism imbalance, excluding the involvement of guanine in BRD4 regulation. We then investigated the effect of these metabolites on RFP expression while degrading BRD4 protein by dBET6[33] treatment or inhibiting BRD4-histone binding ability by (+)-JQ1 treatment in REDS cells. Notably, adenine-related metabolites were then no longer sufficient to decrease RFP expression (Extended Data Fig. 10b, c). Moreover, by examining MYC expression as an additional readout of BRD4 inhibition consequence, we confirmed that adenine-related metabolites could restore MYC expression upon cells with 6-MP treatment. However, no convincing restoration of MYC by supplementing any of these metabolites was observed while inhibiting BRD4 by (+)-JQ1 treatment (Extended Data Fig. 10d), demonstrating that adenine-dependent metabolic regulation is either epistatically upstream of BRD4 or acts directly on BRD4 itself, since none of these metabolites was able to reactivate MYC expression while directly interrupting BRD4-histone binding by (+)-JQ1 treatment.

To further strengthen the above findings, we performed ChIP-qPCR experiments in two other CML cell lines, K562 and LAMA-84, using primer sets targeting *MYC* and *BCL-2* promoter regions that we previously found to be bound by BRD4, as well as a negative control primer set targeting non-BRD4 bound region. The results revealed that impairing purine metabolism by 6-MP treatment or knocking out the three SLCs led to inhibition of BRD4 binding to its target gene loci. Supplementation of adenine, instead of cytidine,

restored the recruitment of BRD4 upon purine impairment, whereas BRD4 functionality was not restored upon (+)-JQ1 treatment (Fig. 5c). In summary, these results highlighted an adenine-dependent metabolic regulation on BRD4-chromatin binding dynamics.

Discussion

How does the environment affect chromatin-dependent cellular states? The growing evidence of the effect of extracellular nutrients and metabolites availability on cellular epigenetic states has raised the untested hypothesis that transporters taking up extracellular nutrients into cells could participate in environment-chromatin crosstalks[34,35]. Several studies have previously implicated intracellular SLCs in epigenetic regulation, particularly by controlling availability of substrates for epigenetic marks. For instance, overexpression of *SLC25A26*, a transporter importing SAM from cytoplasm into the mitochondrial matrix, leads to a rewiring of methionine metabolism and hypermethylation of mitochondrial DNA[36]. Moreover, loss of the mitochondrial citrate carrier *SLC25A1* impairs acetyl-CoA synthesis, thereby affecting global histone acetylation[37]. Whether extracellularly available metabolites could directly affect the function of master epigenetic regulators was less understood. In this study, by integrating an SLC loss-of-function screen and a metabolic compound library screen, we identified a connection between intracellular purine availability and BRD4 function driven by SLC nucleoside transporters. Purine and pyrimidine are both fundamental building blocks of nucleic acids, but only purine supplementation rescued BRD4 functionality in cells growing in the absence of nucleosides or harboring defective nucleosides transport, indicating an additional regulatory role for this class of metabolites.

Extracellular purines, such as adenosine and ATP, are considered prototypical danger signals, as they are released from inflammatory cells as well as cancer cells and accumulate at inflammatory sites[38,39]. Purines are abundant components of the tumor microenvironment, where they may reach concentrations in the high micromolar range[40]. Additionally, extracellular purines acting on purinergic receptors have a major role in modulating immunosuppression and cancer progression[38,39]. Nevertheless, the role of nucleoside transporter-mediating purine uptake in cancer development and in the tumor microenvironment is still unclear. Transporter-mediated uptake of nucleosides across the cell membrane is generally regarded as an alternative pathway to provide building blocks for DNA synthesis[41] but was not known to have a regulatory role. Our findings provide additional insights that the nucleoside transporters mediate the crosstalk between the environment and chromatin states. Loss of nucleoside transporting SLCs, resulting in reduced purine transport into cells, led to a prominent BRD4 inhibition. Overexpression of WT SLCs, but not of transporter defective mutants, rescued this phenotype, suggesting SLC-mediated purine uptake actively supports BRD4 functionality, possibly boosting cancer proliferation in the purine-rich tumor microenvironment. In this context, it is worth mentioning that the purine-nucleoside transporter axis has a critical role in supporting host-cancer interactions[39]. This critical role of purine metabolites in regulating BRD4 functionality was further highlighted by the effect of inhibition of *de novo* purine synthesis.

The balance of intracellular purine pools is maintained by the interplay between purine uptake, *de novo* synthesis, salvage and degradation processes. Generally, salvage pathway accounts for most of the

intracellular purines to economize intracellular energy expenditure. However, upon high requirements for purines, such as during cell proliferation, intracellular purines are replenished by *de novo* synthesis to sustain the increased nucleotides demands[42]. In our study, by knocking out genes involved in purine metabolism, we found that BRD4 functionality was specifically influenced when purine uptake or *de novo* synthesis was inhibited. In this regard, we speculate that purine uptake *via* SLC nucleoside transporters and *de novo* purine synthesis may play predominant roles in maintaining the balance of intracellular purine pools in comparison to salvage and degradation processes, at least in the context of CML models. Notably, uptake of purine from the environment was elevated while *de novo* purine synthesis was inhibited, and inhibition of purine uptake slightly stimulated *de novo* purine synthesis. Although the relative contribution of each purine metabolic process to the intracellular purine pools remains hard to quantify precisely, our findings pointed out a potential reciprocal regulation between purine uptake and *de novo* purine synthesis.

When intracellular purine pools were imbalanced, the association of BRD4 with chromatin was interrupted. In this circumstance, adenine-related metabolites supplementation was able to restore BRD4 functionality, pointing to a specific involvement of adenine in BRD4 biology. Our findings could be due to the essential roles of adenine-related metabolites in maintaining the content of adenylates, functional relevant in a wide array of physiologic processes. Firstly, chromatin remodeling complexes harnessing energy released by adenylates breakdown, such as ATP hydrolysis, has been found as a core control of chromatin architectures, while inhibiting ATPase within the complex precluded transcriptional reprogramming[43,44]. Notably, BRD4 has been shown to localize at gene promoters in concert with SWI/SNF[45], an ATP-dependent chromatin remodeling complex. In line with the close connection between purine metabolism and adenylates generation, it is therefore possible that BRD4-dependent chromatin remodeling was affected upon purine imbalance owing to lower adenylate levels. Secondly, adenylates interconversion is required for protein phosphorylation[46]. The phosphorylation of BRD4 by protein kinases, such as CK2 and CDK1, triggers the interaction of BRD4 and chromatin[45-47]. Treatment of type I kinase inhibitor, an ATP competitor, led to inhibition of BRD4-dependent transcriptional regulation and BETi resistance in cancer cells[48], again demonstrating the indispensable role of adenylates in BRD4 biology. Therefore, adenine-related metabolites supplementation replenished adenylate contents in cells could legitimately reverse either the activity of BRD4-related chromatin remodeling complex or BRD4 phosphorylation. This further raises the concern of the potential involvement of one of the most important adenylates, ATP, in BRD4 regulation. In the metabolic compound library used, several compounds function to impair ATP production, such as FCCP and 3-nitropropionic acid, that respectively interfere with mitochondrial proton gradient and mitochondrial complex II of the electron transport chain (ETC)[49], failed to induce any BRD4 inhibition phenotype at the early timepoint of treatment. However, followed by the strong cytotoxic effect at later timepoints, we were unable to further monitor any effects. On the other hand, it was previously reported that the bromodomains of BRD4 and BRD9 bind purine derivatives[50-52]. It is tempting to speculate that an imbalance of the purine intracellular concentration could affect cellular epigenetic state through the direct binding of a purine or adenine moiety to BRD4 bromodomains or one of the proteins interacting with BRD4[14]. While our attempts to detect such an interaction with known purine metabolites have been unsuccessful so far, alternative approaches, such as a more comprehensive assessment of BRD4-

metabolite interactions by mass spectrometry-based untargeted metabolomics, would be required to shed further light on the mechanism.

BRD4 is considered a compelling target in cancer due to its critical role in cancer progression[11,28]. BETi are being explored as therapeutic agents and currently being pursued in clinical trials (NCT03205176, NCT02705469 and NCT01587703). Although early results from these trials are encouraging, primary and acquired BETi resistance mechanisms have been reported in several preclinical studies[53,54], which could hamper the therapeutic potential of BETi. Using BETi-insensitive leukemia cell lines as a model to investigate the inhibition of *de novo* purine synthesis in the state of primary BETi resistance, we found that 6-MP treatment sensitized these cells to BETi, suggesting that combinatorial treatments involving *de novo* purine synthesis inhibition could serve to circumvent BETi resistance. Further investigation on the role of *de novo* purine synthesis on the interactions with acquired BETi resistance mechanisms, involving extended time scales and mechanistic approaches, should follow.

Our study illustrates a metabolic regulatory axis of BRD4 function driven by purine/adenylate levels maintained by SLC-mediated purine uptake and *de novo* purine synthesis (Fig. 5d). Impairing purine metabolism by (1) depriving purine from the environment, (2) inhibiting purine uptake, or (3) impairing *de novo* purine synthesis leads to BRD4-chromatin disassociation and consequent BRD4 dysfunction. Our findings suggest that inhibition of purine metabolism should further be investigated for its potential use in the treatment for diseases driven by BRD4 dysregulation.

Acknowledgements

We thank all members of the Superti-Furga and Kubicek laboratories for discussions, feedback and reagents, the Platform Austria for Chemical Biology (PLACEBO) for metabolic compound library plating, the Proteomics and Metabolomics Facility for metabolomics analyses and the Biomedical Sequencing Facility for next-generation sequencing. In particular, we would like to thank Andrea Casiraghi for providing valuable feedback. CeMM and the Superti-Furga and Kubicek laboratories are supported by the Austrian Academy of Sciences. We acknowledge receipt of third-party funds from the Austrian Science Fund (FWF SFB F4711, F.K., J.W.B., G.S-F.; I2192-B22 ERASE, V.S.), the European Research Council (ERC AdG 695214 GameofGates, K-C.L., E.G., A.B., U.G., G. S-F.), the European Commission (Marie Sk1odowska-Curie Action Fellowship 661491, E.G.) and an EMBO long-term Fellowship (ALTF 733-2016, T.P.). S.G. is supported by the Peter and Traudl Engelhorn Foundation. Research in the Kubicek lab is supported by the Austrian Science Fund (FWF F4701) and the European Research Council under the European Union's Horizon 2020 research and innovation programme (ERC-CoG-772437).

Author contributions

G.S.-F. conceived the study. K-C.L., E.G., S.K., S.Sdelci and G.S-F. designed the study. K-C.L. performed experiments and analyzed the data. B.G., D.R. and K.K. performed and analyzed the metabolomics experiments. T.P., A.B., J.W.B., J-M.G.L. and S.Schick generated reagents and provided scientific insight. S.Schick helped on ChIP experiment. S.G. analyzed the ChIP-seq data. U.G. analyzed the SLC CRISPR/Cas9

screen data. F.K. established the image-based metabolic compound library screen pipeline and analyzed the data. V.S. analyzed the transcriptomics data. K-C.L., E.G., S. Sdelci and G.S-F. wrote the paper.

Competing interests

G.S.-F, S.K. and A.B. are founders and own shares of Solgate GmbH, an SLC-focused company. S.Sdelci and S.K. have filed patent application WO 2018/087401 A2 on synergistic combinations with BRD4 inhibitors. The other authors declare no competing interests.

Methods

Cell lines

KBM-7 WT cells were obtained from Haplogen. HEK293T and K562, Jurkat E6.1 and Raji cells were purchased from ATCC. LAMA-84 cells were purchased from DSMZ. BRD4 reporter clones (REDS) were generated by retroviral-based gene trap technology as previously described[15,16] using the human male near-haploid CML cell line KBM-7. REDS1, REDS15, REDS17 and KBM-7 WT cells were maintained in Iscove's Modified Dulbecco's Medium (IMDM, Gibco). Jurkat E6.1, Raji, K562 and LAMA-84 were maintained in RPMI 1640. HEK293T cells were maintained in Dulbecco's Modified Eagles Medium (DMEM, Gibco). All media were supplemented with 10% Fetal Bovine Serum (FBS, Gibco) and 1% penicillin/streptomycin (PS). cell lines were maintained at 5% CO_2 at 37°C, initially authenticated by STR typing before use (except the REDS) and tested for mycoplasma contamination.

Plasmids and cloning

CRISPR/Cas9-based SLC KO cell generation was performed using the pLentiCRISPRv2 vector (Addgene #52961) containing a modified tracrRNA variant (pLentiCRISPRv3)[55], pLentiGuide-BlastR and pLentiGuide-NeoR vectors were derived in-house by replacing the PuroR resistance cassette with BlastR or NeoR in the pLentiGuide-PuroR vector (Addgene #52963). In brief, sgRNAs for each gene were designed using the CHOPCHOP prediction tool[56]. Oligonucleotides containing *BsmBI* restriction site-compatible overhangs were annealed, phosphorylated and ligated into above listed vectors using standard cloning techniques and sequence verified using Sanger sequencing. sgRNAs targeting purine metabolism were cloned into pLentiCRISPRv2 (Addgene #52961). Sequences of sgRNA are listed in Supplementary Table 3. Codon-optimized sgRNA-resistance SLC28A3 and SLC29A4 plasmids were synthesized by GeneScript (Supplementary Table 4). After sequence verification, the cDNAs were cloned into pDONR221 plasmid and then subcloned into pRRL-based lentiviral expression plasmids containing a N- or C-terminal StrepII-HA tag and a BlastR resistance cassette[57] using the Gateway cloning system (Thermo Fisher Scientific). Transporter defective mutants SLC28A3 G367R and SLC29A4 I89M were generated using NEB Q5 site-directed mutagenesis kit (Supplementary Table 4).

RFP integration locus analysis in REDS cells

RFP integration site in REDS1 cells has been identified in ref[14]. In REDS15 and REDS17 clones, the genomic integration locus was further identified by using Retro-X™ Integration Site Analysis Kit (Clontech Laboratories) according to the instructions provided by the manufacturer.

SLC KO CRISPR/Cas9 screen and cell sorting

The SLC knockout CRISPR/Cas9 library has been described previously by Girardi et al.[15] (Addgene #132552). Briefly, a CRISPR/Cas9 library targeting 388 SLCs and 6 SLC pseudogenes with 6 guides per gene, together with 120 guides targeting 20 essential genes and 120 non-targeting or control guides, was cloned by Gibson cloning in the pLentiCRISPRv2 (Addgene #52961). Viral particles were generated by transient transfection of HEK293T cells with the library and packaging plasmids pMD2.G (Addgene #12259) and psPAX2 (Addgene #12260) using PolyFect (Qiagen). 24 hours after transfection, the medium was changed to fresh IMDM

supplemented with 10% FBS. The viral supernatant was collected after 72 hours of transfection, filtered and stored at -80ºC until further use. REDS1, REDS15 and REDS17 clones were infected in triplicates by the viral supernatant at a low multiplicity of infection (MOI around 0.3, library coverage ~2000x) to allow for integration of a single lentiviral sgRNA cassette per cell. The infected cells were selected with 0.5 µg/ml puromycin for 7 days, then grown in puromycin-free medium for 2 days before sorting. Approximately 50,000 of the highest 0.5% RFP-expressing cells were sorted by using FACSAria (BD Biosciences) sorter and expanded to 6 million cells. Genomic DNA was extracted using the QIAamp DNA Mini Kit (Qiagen). The sgRNA inserts in the input control cell populations as well as sorted samples were PCR-amplified using barcode-containing primers (IDT Ultramers) as described previously[15], the indexed samples were subsequently pooled and sequenced on a HiSeq 3000/4000 (Illumina) at the Biomedical Sequencing Facility (BSF at CeMM, https://biomedical-sequencing.at).

SLC knockout CRISPR/Cas9 screen data analysis

RNA-Seq reads were demultiplexed and mapped to the sgRNAs present in the library using a custom procedure implemented in Python (crispyCount). Samples with a median sgRNA coverage of less than 10 were excluded from further analysis (4 out of 18 samples). To compensate for the noise and off target action of sgRNAs inherent to CRISPR screening approaches, we used a two-step differential abundance analysis. In a first step, differential abundance of sgRNAs in sorted samples compared to unsorted samples, across biological replicates and clones, was estimated with DESeq2 library (version 1.22.2)[58]. Subsequently, significantly enriched sgRNAs (adjusted p-value ≤ 0.05) were sorted by fold change and aggregated to genes using Gene Set Enrichment Analysis with fgsea library (version 1.8.0)[59], requiring at least two significant guides per gene. Resulting enriched SLC genes were filtered for expression based on 3'mRNA sequencing analysis, with the normalized raw counts > 0, sorted by decreasing significance and the top 16 candidates were considered hits (corresponding to a p-value ≤ 0.171).

Flow cytometry

The RFP expression which represents BRD4 inhibition phenotype was measured on LSR Fortessa II cytometer interfaced with FACSDiva (BD Biosciences). Live cells were gated based on the FSC-A and SSC-A, followed by FSC-A and FSC-H gating to select the singlet cells. FlowJo software version 10 (Tree Star) was used for data analysis.

Metabolic compound library screen

The custom-made metabolic drug library will be described in detail in Pemovska et al. (in preparation). During the screen, 1 µM (+)-JQ1 was used as positive control and DMSO and 1 µM (-)-JQ1 were included as negative and vehicle controls, respectively. Three REDS clones and KBM-7 cells were treated with 10 µM of each compound. Briefly, 2.5 nl of DMSO, 1mM (+)-JQ1, 1mM (-)-JQ1 and 10 mM compounds were transferred from a 384-well compound library source plate to 384-well tissue-culture treated black microplates with optically clear bottom (Perkin Elmer) by a Labcyte Echo liquid handler attached to a Perkin Elmer high-content cell::explorer workstation (PLACEBO lab at CeMM). 20,000 cells in 25 µl IMDM supplemented with 10% FBS and 1% PS were further seeded in the plates and images with 20X magnification were taken by automated

microscopy Opera Phenix High-Content Screening System (Perkin Elmer). 5 images were taken per well every 24 hours until 96 hours treatment. Automated image analysis was performed using CellProfiler 2.1.2[60]. In brief, bright field images were smoothed using a Gaussian filter and cells, represented as dark structures with a light ring like halo, were enhanced as dark hole features in the smoothed images. Cells were thereafter identified from enhanced features to quantify cellular RFP intensity and cellular morphology. In addition, information about total RFP intensity, mean cell area as well as the cell count per image was collected. Consecutive analysis and plotting were performed in R (version 3.4.4).

Western blot analysis

Cells were lysed in RIPA lysis buffer (50 mM Tris (pH 8.0), 150 mM NaCl, 5 mM EDTA, 1% NP-40, sodium deoxycholate 0.5%, 0.1% SDS, with one tablet of EDTA-free protease inhibitor (Roche) per 50 ml) for 20 min on ice, then centrifuged at 20800 g at 4°C for 15 min to remove the cell debris. Protein concentration was measured with BCA (Pierce) and samples were separated by sodium dodecyl sulfate–polyacrylamide gel electrophoresis and transferred to nitrocellulose membranes (GE Healthcare). The membranes were further blocked with 5% milk in TBS-T, then incubated with indicated antibodies. After peroxidase coupled secondary antibodies incubation, the anti-bound proteins were visualized ECL Western blotting system (Thermo Scientific), according to the instructions.

Antibodies list

The primary antibodies for western blot were: HA (901501, BioLegend, dilution 1:5000), BRD4 (ab128874, Abcam, dilution 1:2500), α-Tubulin (ab7291, Abcam, dilution 1:10000), Lamin B1 (ab16048, Abcam, dilution 1:2500), Histone H3 (ab18521, Abcam, dilution 1:2500), H3K27ac (8173, Cell Signaling, dilution 1:2500), Pan-acetyl H3 (39140, Active Motif, dilution 1:2500), MYC (sc-40, Santa Cruz, dilution 1:500) and GAPDH (sc-365062, Santa Cruz, dilution 1:10000). The secondary antibodies used were goat anti-mouse HRP (115-035-003, Jackson ImmunoResearch, dilution 1:5000), goat anti-rabbit HRP (111-035-144, Jackson ImmunoResearch, dilution 1:5000). Antibodies used for ChIP-seq and ChIP-qPCR were: BRD4 (ab128874, Abcam) and rabbit polyclonal IgG (sc-66931, Santa Cruz).

Metabolites profiling and LC-MS analysis

For metabolites collection, 20 million cells per replicates were washed by PBS and incubated in FBS-free IMDM for 30 min in 5% CO_2 atmosphere at 37°C. Cells were further washed twice with cold PBS, lysed with 1 ml cold Methanol:H_2O solution (80:20) and centrifuged at 20800 g at 4°C for 15 min. The supernatant was collected and immediately snap frozen. For the targeted metabolomics experiments, the cell extract samples were dried down using nitrogen evaporator and reconstituted in 100 µl of methanol. Samples were vortexed for 10 seconds and centrifuged at 1000 g for 10 min. 15 µl of supernatant were mixed with 10 µl of isotopically labelled internal standards, followed by the addition of 5 µl of water and 150 µl of methanol. Samples were vortexed for 10 seconds and centrifuged at 1000 g for 10 min. The supernatant was collected and used for LC-MS analysis (Pro-Met, CeMM). A Vanquish UHPLC system (Thermo Scientific) coupled with an Orbitrap Q Exactive (Thermo Scientific) mass spectrometer was used for the LC-MS analysis. The chromatographic separation for samples was carried out on an ACQUITY UPLC BEH Amide, 1.7 µm, 2.1x100 mm analytical

column (Waters) equipped with a VanGuard: BEH C18, 2.1x5mm pre-column (Waters). The column was maintained at a temperature of 40°C and 2 µl sample were injected per run. The mobile phase A was 0.15% formic acid (v/v) in water and mobile phase B was 0.15% formic acid (v/v) in 85% acetonitrile (v/v) with 10 mM ammonium formate. The gradient elution with a flow rate 0.4 mL/min was performed with a total analysis time of 17 min. The Orbitrap Q Exactive (Thermo Scientific) mass spectrometer was operated in an electrospray ionization positive mode, spray voltage 3.5 kV, aux gas heater temperature 400°C, capillary temperature 350°C, aux gas flow rate 12. The metabolites of interest were analyzed using a full MS scan mode, scan range m/z 50 to 400, resolution 35000, AGC target 1e6, maximum IT 50ms. The Trace Finder 4.1 software (Thermo Scientific) was used for the data processing. Seven-point linear calibration curves with internal standardization and 1/x weighing was constructed for the quantification of metabolites.

Stable isotope labeled adenine and glycine incorporation into nucleic acid and LC-MS analysis

REDS15 cells were treated with growth medium containing 50 µM 8-^{13}C-adenine (+1) (CLM-1654-PK, Cambridge Isotope Laboratories) or ^{13}C2-^{15}N-glycine (+3) (CNLM-1673-H-PK, Cambridge Isotope Laboratories) and incubated for 24 h. RNA was extracted from cells using RNeasy Mini kit (Qiagen) according to manufacturer's instructions and the concentration was measured using a Nanodrop spectrophotometer. After alkaline hydrolysis, samples were equilibrated with NaOH. 10 µl of hydrolysed RNA samples were mixed with 40 µl of methanol. Afterwards, samples were vortexed for 10 seconds, incubate on ice for 5 min, vortexed for 10 seconds and centrifuged at 1000 g for 10 min. The supernatant was collected and used for LC-MS analysis (Pro-Met, CeMM). A Vanquish UHPLC system (Thermo Scientific) coupled to an Orbitrap Fusion Lumos (Thermo Scientific) mass spectrometer was used for the LC-MS analysis. The chromatographic separation for samples was carried out on an ACQUITY UPLC BEH Amide, 1.7 µm, 2.1x100 mm analytical column (Waters) equipped with a VanGuard: BEH C18, 2.1x5mm pre-column (Waters). The column was maintained at a temperature of 40°C and 2 µl sample were injected per run. The mobile phase A was 0.15% formic acid (v/v) in water and mobile phase B was 0.15% formic acid (v/v) in 85% acetonitrile (v/v) with 10 mM ammonium formate. The gradient elution with a flow rate 0.4 mL/min was performed with a total analysis time of 17 min. The mass spectrometer was operated in a positive electrospray ionization mode: spray voltage 3.5 kV; sheath gas flow rate 60 arb; auxillary gas flow rate 20 arb; capillary temperature 285 °C. For the analysis a full MS scan mode with a scan range m/z 110 to 500, resolution 120000, AGC target 2e5 and a maximum injection time 50 ms was applied. The data processing was performed with the TraceFinder 4.1 software (Thermo Scientific).

Chromatin-bound protein enrichment and cell fractionation

Pellets from 15 million cells were lysed in 150 µl cold cytoplasmic lysis buffer (0.15% NP-40, 10 mM Tris-HCl pH 7.0, 50 mM NaCl and protease inhibitor). After 5 min on ice incubation, the lysates were layered onto 400 µl cold sucrose buffer (10 mM Tris-HCl pH 7.0, 150 mM NaCl, 25% sucrose and protease inhibitor) and centrifuged for 10 min at 18000 g at 4ºC. The supernatant was harvested as cytoplasmic fraction, and pellets were further washed by 1 ml cold-nuclei wash buffer (0.1% triton X-100, 1 mM EDTA, 1X PBS and protease inhibitor) followed by spinning down for 5 min at 1300 g at 4ºC for 3 times. Pellets were further gently

resuspended in 200 µl cold glycerol buffer (20 mM Tris-HCl pH 8.0, 75 mM NaCl, 0.5 mM EDTA, 50% glycerol, 0.85 mM DTT and protease inhibitor) and mixed with 200 µl cold nuclei lysis buffer (1% NP-40, 20 mM HEPES pH 7.5, 300 mM NaCl, 0.2 mM EDTA, 1 M Urea, 1 mM DTT and protease inhibitor) by pulsed vortexing. After 2 min on ice incubation, the lysates were centrifuged for 2 min at 20800 g at 4ºC, and the supernatant was harvested as nucleoplasmic fraction. The pellets were further resuspended in 100 µl RIPA buffer, sonicated 3 times for 1 sec at ca. 25% intensity, and centrifuged for 10 min at 20800 g at 4ºC. After this step, the supernatant was harvest as chromatin-bound protein fraction. 15 µl cytoplasmic fraction, 12 µl nucleoplasmic fraction and 3 µl chromatin-bound protein fraction were further applied to western blot analysis.

3'mRNA sequencing and data analysis

The Illumina compatible library was prepared with QuantSeq 3'mRNA-seq Library Prep kit (Lexogen) according to manufacturer's instructions. The multiplexed libraries were sequenced on 50-bp single read configuration on a HiSeq 4000 (Illumina) by Biomedical Sequencing Facility at CeMM. Raw sequencing reads were demultiplexed, and after barcode, adaptor and quality trimming with cutadapt (https://cutadapt.readthedocs.io/en/stable/), quality control was performed using FastQC (http://www.bioinformatics.babraham.ac.uk/projects/fastqc/). The remaining reads were mapped to the GRCh38/h38 human genome assembly using genomic short-read RNA-Seq aligner STAR version 2.5. We obtained more than 98 % mapped reads in each sample with 70 – 80 % of reads mapping to unique genomic location. Transcripts were quantified using End Sequence Analysis Toolkit (ESAT). Differential expression analysis was performed using independent triplicates with DESeq2 (1.24.0) on the basis of read counts. Exploratory data analysis and visualizations were performed in R-project version 3.4.2 (Foundation for Statistical Computing, Vienna, Austria, https://www.R-project.org/) with Rstudio IDE version 1.2.1578, ggplot2 (3.3.0), dplyr (0.8.5), readr (1.3.1), gplots (3.0.1).

Chromatin Immunoprecipitation (ChIP)

ChIP experiment was carried out as described in ref[61] and each of the treatment was performed in triplicates. In brief, 50 million cells were crosslinked with 1% formaldehyde for 10 min at room temperature followed by quenching with 125 mM glycine (pH 2.5) for 5 min on ice. After two times washing with cold PBS, cell pellet was lysed and then the chromatin was sheared using a Covaris S2X (duty cycle: 5%; intensity: 4; power: 10 W; cycles per burst: 200; time: 40 min). The fragmented chromatin was incubated with antibodies (4.5 µg) overnight at 4 °C, followed by a 3 h incubation with Dynabeads Protein G (Thermal Fisher Scientific) at 4 °C. After washing the beads twice with low-salt RIPA buffer, twice with high-salt RIPA buffer and twice with RIPA-LiCl buffer, the antibody-bound chromatin was eluted, and treated with RNase for 30 min at 37 °C, with proteinase K for 2.5 h at 55°C, and then decrosslinked overnight at 65 °C. DNA was then extracted using phenol-chloroform, precipitated and then dissolved in Tris-EDTA buffer. For ChIP-sequencing, the libraries were prepared using NEBNext Ultra II DNA Library Prep Kit for Illumina (New England Biolabs, E7645S) with NEBNext Multiplex Oligos for Illumina (New England Biolabs, E7335S and E7500S) according to manufacturer's instructions. The libraries were sequenced on 50-bp single read configuration on a HiSeq 4000 (Illumina) by Biomedical Sequencing Facility at CeMM.

Pre-processing of ChIP-seq reads and bioinformatic analyses

Read trimming was performed using Skewer[62]. Read mapping was performed to GRCh38/hg38 using Bowtie2[63] and the "-very sensitive" parameter. Only unique reads with a mapping quality >30 and alignment to the nuclear genome were included in the downstream analyses. Peak calling was performed using MACS2[64] using respective IgG ChIP samples as control. Peaks overlapping blacklisted features defined in the ENCODE project38 were discarded from the analyses. Consensus peak set generation of ChIP-seq peaks across samples per ChIP-seq dataset, read count quantification per peak and read count normalization across samples using reads per million normalization (rpm) was performed as implemented in ngs.toolkit (https://github.com/afrendeiro/toolkit). ChIP-seq consensus peaks were annotated to their closest gene body as implemented in ngs.toolkit (https://github.com/afrendeiro/toolkit). Principal component analysis (PCA) was performed using the R package factoextra (https://CRAN.R-project.org/package=factoextra).

Three replicates per sample were available for analysis except for 6-MP treatment where replicate number 3 (6-MP_BRD4_IP_rep3) in REDS15 cells was excluded after PCA analysis (Extended Data Fig. 6a). Differential expression analysis was performed using DESeq2[58] using raw count data. Differential regions were defined as having an FDR-adjusted *p*-value <0.01 and an absolute $\log_2$ fold change >= 1. Aggregate coverage plots and chromatin accessibility heatmaps were generated using plotHeatmap and plotProfile functions implemented in the deepTools package[65].

RNA extraction, RT-qPCR and ChIP-qPCR

Total RNA was extracted using RNeasy Mini kit (Qiagen) including a DNase I digest step according to manufacturer's instructions and the reverse transcription was performed using RevertAid reverse transcriptase (Thermo Fisher Scientific) together with oligo dT primers. The RT-qPCR and ChIP-qPCR experiments were performed using SensiFAST SYBR Green (Bioline) analyzed on a Rotor-Gene Q (Qiagen). The results of RT-qPCR on *MYC* expression were normalized to *GAPDH*. ChIP-qPCR was performed for quantification of the enrichment of BRD4 at *MYC* and *BCL-2* promoter regions. Enrichment data were analyzed by calculating the immunoprecipitated DNA percentage of input DNA for each sample. Primer sequences are listed in Supplementary Table 5.

Cell viability assay

Cell viability was determined using CellTiter Glo Luminescent Cell Viability Assay (Promega) on quantitation of the ATP present according to the instructions provided by the manufacturer, or by CASY Cell Counter and Analyzer (Innovatis) on counting the cell numbers in triplicates. Luminescent output from CellTiter Glo was recorded by SpectraMax M5 Multimode plate reader (Molecular Devices).

Statistics and reproducibility

All the experiments were performed with at least two biological replicates. Western blot experiments were performed two times independently with similar results.

Data availability

ChIP-seq and RNA-seq data have been deposited to NCBI GEO (GSE167374, GSE168099 and GSE168101).

Figure legends

Fig. 1. A SLC-focused CRISPR/Cas9 genetic screen identifies a functional link between SLC nucleoside transporters and BRD4. a, Schematic overview of FACS-based SLC loss-of-function screen in REDS clones. **b,** The enrichment of sgRNA-targeted SLCs in the highest 0.5% RFP-expressing REDS cells versus the unsorted population. The color-coded dots represent the top 16 enriched SLCs from the screen according to -$\log_{10}$(*p*-value). **c,** Validation of individual hits by SLC knockout. REDS1 and REDS15 cells were infected with lentivirus-based sgRNA expression cassettes and the RFP intensity was measured 12 days after sgRNA transduction. The $\log_2$ fold change of RFP intensity was calculated relatively to the cells transduced with control sgRNA (sg*Ren*). Mean ± s.d., n =3 biologically independent samples. The *p*-value was calculated by paired *t*-tests. **d,** RFP expression in REDS15 cells with the identified SLC hits single, dual or triple knockout (SLC TKO) after sgRNA transduction for 12 days. **e,** RFP expression in REDS15 cells with SLC knockout exogenously supplied with purine (adenosine and guanosine) or pyrimidine (cytidine and thymidine) nucleosides for 72 h. The $\log_2$ fold change of RFP intensity was calculated relatively to sg*Ren* cells with DMSO treatment. Mean ± s.d., n =3 biologically independent samples. **f,** Western blot analysis of the overexpression level of N- or C-terminal HA-tagged wild-type (WT) or transporter activity defective mutant SLC28A3 or SLC29A4 in REDS15 cells with respective SLC knockout. **g,** RFP expression in REDS15 cells as indicated.

Fig. 2. Metabolic perturbation on *de novo* purine synthesis leads to BRD4 inhibition. a, Schematic overview of image-based metabolic compound library screen. **b,** Image-based quantification of cellular RFP induction upon metabolic compound library treatment in REDS1, REDS15, REDS17 and KBM-7 WT cells over time. The $\log_2$ fold change in mean cellular RFP signal, relative to DMSO per time point (Y-axis), plotted against the numbers of cells detected per image (X-axis), color-coded for mean cell area (pixels/cell, 1 px = 0.35 μm^2) as a surrogate for cell viability. **c,** Catabolism of azathioprine and 6-MP. **d,** RFP expression in REDS15 cells with indicated concentrations of 6-MP-related compounds treatment for 72 h. **e,** RFP expression in REDS15 cells with purine metabolism genes knockout. The $\log_2$ fold change of RFP intensity was calculated relatively to sg*Ren* cells. Mean ± s.d., n =3 biologically independent samples. The *p*-value was calculated by unpaired *t*-tests.

Fig. 3. Impairing purine metabolism by blocking nucleoside uptake or *de novo* purine synthesis results in BRD4 inhibition. a, Metabolite composition in REDS15 cells with triple SLC knockout (SLC TKO) 12 days after sgRNA transduction, 10 μM 6-MP or 1 μM (+)-JQ1 treatment for 48 h. The $\log_2$ fold change of metabolites level was calculated relatively to sg*Ren* or DMSO treated cells. AA, amino acids; NT, nucleotides; NB, nucleobases; NS, nucleosides. **b,** Western blot analysis of BRD4 expression in chromatin-bound, nucleoplasm and cytoplasmic fractions in REDS15 cells. Lamin B1, GAPDH and histone H3 were markers for nuclear-chromatin, cytoplasm and chromatin-bound protein fractions. ns, non-specific band. **c,** Heatmaps representing BRD4 binding enrichment for all ChIP-seq consensus peak regions (N = 24,140). **d,** Aggregate coverage plots showing mean enrichment for the different ChIP-seq consensus peak regions in REDS15 cells with 10 μM 6-MP or 1 μM (+)-JQ1 treatment or bearing triple SLC knockout (SLC TKO), with ±10 kb centered on the regions. **e,** Genome browser visualization of BRD4 binding at its representative target genes *MYC* and

BCL-2 in REDS15 cells with indicated treatments. The graphs from ChIP-seq experiment shown here are the merged results of the replicates.

Fig. 4. SLC-mediated purine uptake and *de novo* purine synthesis converge on BRD4 regulation. a,**b**, Relative RFP intensity (**a**) and cell viability (**b**) of SLC28A3 or SLC29A4 overexpressing REDS15 cells with or without *PPAT* knockout 10 days after sgRNA transduction. Mean ± s.d., n=3 biologically independent samples. The *p*-value was calculated by unpaired *t*-tests. **c**,**d**, Relative RFP expression (**c**) and cell viability (**d**) of REDS15-sg*PPAT* cells with nucleosides supplement for 72 h. Mean ± s.d., n=3 biologically independent samples. **e**, Stable isotope labeled +1 adenine or +3 glycine tracing into nucleotides in REDS15 vehicle cells, with triple SLC knockout (SLC TKO, 12 days after sgRNA transduction) or with 10 μM 6-MP treatment after 24 h. Mean ± s.d., n=3 biologically independent samples. The *p*-value was calculated by unpaired *t*-tests. **f,g,** Relative RFP intensity (**f**) and cell viability (**g**) of REDS15 cells with *PPAT*, triple SLC knockout (SLC TKO, 12 days after sgRNA transduction) or the combined knockout. Mean ± s.d., n=3 biologically independent samples. The *p*-value was calculated by unpaired *t*-tests. Cell viability was measured by CellTiter Glo assay. **h,** RFP expression in control sg*Ren* cells and cells with triple SLC knockout (SLC TKO, 12 days after sgRNA transduction) treated with DMSO or 1 uM (+)-JQ1 for 72 h. **i,** Dose-response matrix displaying the RFP intensity in REDS1 and REDS15 clones treated with indicated concentrations of (+)-JQ1 or 6-MP, or in combination for 72 h, relative to treatment with DMSO.

Fig. 5. Adenine-containing nucleotides supplementation rescues BRD4 functionality upon purine metabolism impairment. a, Relative RFP expression in REDS cells with triple SLC knockout (SLC TKO, 12 days after sgRNA transduction) supplemented with indicated concentrations of nucleotide metabolites for 72 h. The $\log_2$ fold change was calculated relatively to sg*Ren* cells with DMSO treatment. **b,** Relative RFP expression in REDS cells with 10 μM 6-MP and indicated concentrations of nucleotide metabolites co-treatment for 72 h. The $\log_2$ fold change was calculated relatively to cells treated with DMSO. **c**, ChIP-qPCR analysis using primers targeting BRD4-bound *MYC* and *BCL-2* promoter regions and non-bound *MYC* super enhancer upstream in K562 and LAMA-84 cells treated with DMSO, 10 μM 6-MP, 1 μM (+)-JQ1 or cells bearing triple SLC knockout (SLC TKO), with or without 100 μM adenine or cytidine supplementation for 72 h. Enrichment was shown as the percentage of total input DNA of each sample. Mean ± s.d., n=2 biologically independent samples. **d,** Proposed mechanism of purine metabolism in BRD4 regulation.

References

1 Flavahan, W. A., Gaskell, E. & Bernstein, B. E. Epigenetic plasticity and the hallmarks of cancer. *Science* **357**, doi:10.1126/science.aal2380 (2017).

2 Sharma, S., Kelly, T. K. & Jones, P. A. Epigenetics in cancer. *Carcinogenesis* **31**, 27-36, doi:10.1093/carcin/bgp220 (2010).

3 Egger, G., Liang, G., Aparicio, A. & Jones, P. A. Epigenetics in human disease and prospects for epigenetic therapy. *Nature* **429**, 457-463, doi:10.1038/nature02625 (2004).

4 Ulrey, C. L., Liu, L., Andrews, L. G. & Tollefsbol, T. O. The impact of metabolism on DNA methylation. *Hum Mol Genet* **14 Spec No 1**, R139-147, doi:10.1093/hmg/ddi100 (2005).

5 Jenuwein, T. & Allis, C. D. Translating the histone code. *Science* **293**, 1074-1080, doi:10.1126/science.1063127 (2001).

6 Cesar-Razquin, A. *et al.* A Call for Systematic Research on Solute Carriers. *Cell* **162**, 478-487, doi:10.1016/j.cell.2015.07.022 (2015).

7 Hediger, M. A. *et al.* The ABCs of solute carriers: physiological, pathological and therapeutic implications of human membrane transport proteinsIntroduction. *Pflugers Arch* **447**, 465-468, doi:10.1007/s00424-003-1192-y (2004).

8 Zhang, Y., Zhang, Y., Sun, K., Meng, Z. & Chen, L. The SLC transporter in nutrient and metabolic sensing, regulation, and drug development. *J Mol Cell Biol* **11**, 1-13, doi:10.1093/jmcb/mjy052 (2019).

9 Rebsamen, M. *et al.* SLC38A9 is a component of the lysosomal amino acid sensing machinery that controls mTORC1. *Nature* **519**, 477-481, doi:10.1038/nature14107 (2015).

10 Song, W., Li, D., Tao, L., Luo, Q. & Chen, L. Solute carrier transporters: the metabolic gatekeepers of immune cells. *Acta Pharm Sin B* **10**, 61-78, doi:10.1016/j.apsb.2019.12.006 (2020).

11 Zuber, J. *et al.* RNAi screen identifies Brd4 as a therapeutic target in acute myeloid leukaemia. *Nature* **478**, 524-528, doi:10.1038/nature10334 (2011).

12 Delmore, J. E. *et al.* BET bromodomain inhibition as a therapeutic strategy to target c-Myc. *Cell* **146**, 904-917, doi:10.1016/j.cell.2011.08.017 (2011).

13 Sdelci, S. *et al.* Mapping the chemical chromatin reactivation landscape identifies BRD4-TAF1 cross-talk. *Nat Chem Biol* **12**, 504-510, doi:10.1038/nchembio.2080 (2016).

14 Sdelci, S. *et al.* MTHFD1 interaction with BRD4 links folate metabolism to transcriptional regulation. *Nat Genet* **51**, 990-998, doi:10.1038/s41588-019-0413-z (2019).

15 Girardi, E. *et al.* A widespread role for SLC transmembrane transporters in resistance to cytotoxic drugs. *Nat Chem Biol*, doi:10.1038/s41589-020-0483-3 (2020).

16 Young, J. D., Yao, S. Y., Baldwin, J. M., Cass, C. E. & Baldwin, S. A. The human concentrative and equilibrative nucleoside transporter families, SLC28 and SLC29. *Mol Aspects Med* **34**, 529-547, doi:10.1016/j.mam.2012.05.007 (2013).

17 Meixner, E. *et al.* A substrate-based ontology for human solute carriers. *Mol Syst Biol* **16**, e9652, doi:10.15252/msb.20209652 (2020).

18 Tandio, D., Vilas, G. & Hammond, J. R. Bidirectional transport of 2-chloroadenosine by equilibrative nucleoside transporter 4 (hENT4): Evidence for allosteric kinetics at acidic pH. *Sci Rep* **9**, 13555, doi:10.1038/s41598-019-49929-w (2019).

19 Ishida, N. & Kawakita, M. Molecular physiology and pathology of the nucleotide sugar transporter family (SLC35). *Pflugers Arch* **447**, 768-775, doi:10.1007/s00424-003-1093-0 (2004).

20 Ahuja, S. & Whorton, M. R. Structural basis for mammalian nucleotide sugar transport. *Elife* **8**, doi:10.7554/eLife.45221 (2019).

21 Matsuyama, R. *et al.* Predicting 5-fluorouracil chemosensitivity of liver metastases from colorectal cancer using primary tumor specimens: three-gene expression model predicts clinical response. *Int J Cancer* **119**, 406-413, doi:10.1002/ijc.21843 (2006).

22 Badagnani, I. *et al.* Functional analysis of genetic variants in the human concentrative nucleoside transporter 3 (CNT3; SLC28A3). *Pharmacogenomics J* **5**, 157-165, doi:10.1038/sj.tpj.6500303 (2005).

23 Ho, H. T., Xia, L. & Wang, J. Residue Ile89 in human plasma membrane monoamine transporter influences its organic cation transport activity and sensitivity to inhibition by dilazep. *Biochem Pharmacol* **84**, 383-390, doi:10.1016/j.bcp.2012.04.018 (2012).

24 Cara, C. J. *et al.* Reviewing the mechanism of action of thiopurine drugs: towards a new paradigm in clinical practice. *Med Sci Monit* **10**, RA247-254 (2004).

25 Kamynina, E. *et al.* Arsenic trioxide targets MTHFD1 and SUMO-dependent nuclear de novo thymidylate biosynthesis. *Proc Natl Acad Sci U S A* **114**, E2319-E2326, doi:10.1073/pnas.1619745114 (2017).

26 Liu, Y. C. *et al.* Global regulation of nucleotide biosynthetic genes by c-Myc. *PLoS One* **3**, e2722, doi:10.1371/journal.pone.0002722 (2008).

27 Donati, B., Lorenzini, E. & Ciarrocchi, A. BRD4 and Cancer: going beyond transcriptional regulation. *Mol Cancer* **17**, 164, doi:10.1186/s12943-018-0915-9 (2018).

28 Donato, E. *et al.* Compensatory RNA polymerase 2 loading determines the efficacy and transcriptional selectivity of JQ1 in Myc-driven tumors. *Leukemia* **31**, 479-490, doi:10.1038/leu.2016.182 (2017).

29 Nigam, S. K. What do drug transporters really do? *Nat Rev Drug Discov* **14**, 29-44, doi:10.1038/nrd4461 (2015).

30 Foucquier, J. & Guedj, M. Analysis of drug combinations: current methodological landscape. *Pharmacol Res Perspect* **3**, e00149, doi:10.1002/prp2.149 (2015).

31 Di Veroli, G. Y. *et al.* Combenefit: an interactive platform for the analysis and visualization of drug combinations. *Bioinformatics* **32**, 2866-2868, doi:10.1093/bioinformatics/btw230 (2016).

32 Wang, C. *et al.* Dipyridamole analogs as pharmacological inhibitors of equilibrative nucleoside transporters. Identification of novel potent and selective inhibitors of the adenosine transporter function of human equilibrative nucleoside transporter 4 (hENT4). *Biochem Pharmacol* **86**, 1531-1540, doi:10.1016/j.bcp.2013.08.063 (2013).

33 Winter, G. E. *et al.* BET Bromodomain Proteins Function as Master Transcription Elongation Factors Independent of CDK9 Recruitment. *Mol Cell* **67**, 5-18 e19, doi:10.1016/j.molcel.2017.06.004 (2017).

34 Shimazu, T. *et al.* Suppression of oxidative stress by beta-hydroxybutyrate, an endogenous histone deacetylase inhibitor. *Science* **339**, 211-214, doi:10.1126/science.1227166 (2013).

35 Mentch, S. J. *et al.* Histone Methylation Dynamics and Gene Regulation Occur through the Sensing of One-Carbon Metabolism. *Cell Metab* **22**, 861-873, doi:10.1016/j.cmet.2015.08.024 (2015).

36 Menga, A. *et al.* SLC25A26 overexpression impairs cell function via mtDNA hypermethylation and rewiring of methyl metabolism. *FEBS J* **284**, 967-984, doi:10.1111/febs.14028 (2017).

37 Morciano, P. *et al.* A conserved role for the mitochondrial citrate transporter Sea/SLC25A1 in the maintenance of chromosome integrity. *Hum Mol Genet* **18**, 4180-4188, doi:10.1093/hmg/ddp370 (2009).

38 Di Virgilio, F. Purines, purinergic receptors, and cancer. *Cancer Res* **72**, 5441-5447, doi:10.1158/0008-5472.CAN-12-1600 (2012).

39 Di Virgilio, F. & Adinolfi, E. Extracellular purines, purinergic receptors and tumor growth. *Oncogene* **36**, 293-303, doi:10.1038/onc.2016.206 (2017).

40 Pellegatti, P. *et al.* Increased level of extracellular ATP at tumor sites: in vivo imaging with plasma membrane luciferase. *PLoS One* **3**, e2599, doi:10.1371/journal.pone.0002599 (2008).

41 Pastor-Anglada, M. & Perez-Torras, S. Emerging Roles of Nucleoside Transporters. *Front Pharmacol* **9**, 606, doi:10.3389/fphar.2018.00606 (2018).

42 Yin, J. *et al.* Potential Mechanisms Connecting Purine Metabolism and Cancer Therapy. *Front Immunol* **9**, 1697, doi:10.3389/fimmu.2018.01697 (2018).

43 Hasan, N. & Ahuja, N. The Emerging Roles of ATP-Dependent Chromatin Remodeling Complexes in Pancreatic Cancer. *Cancers (Basel)* **11**, doi:10.3390/cancers11121859 (2019).

44 Hargreaves, D. C. & Crabtree, G. R. ATP-dependent chromatin remodeling: genetics, genomics and mechanisms. *Cell Res* **21**, 396-420, doi:10.1038/cr.2011.32 (2011).

45 Conrad, R. J. *et al.* The Short Isoform of BRD4 Promotes HIV-1 Latency by Engaging Repressive SWI/SNF Chromatin-Remodeling Complexes. *Mol Cell* **67**, 1001-1012 e1006, doi:10.1016/j.molcel.2017.07.025 (2017).

46 Kole, H. K., Abdel-Ghany, M. & Racker, E. Specific dephosphorylation of phosphoproteins by protein-serine and -tyrosine kinases. *Proc Natl Acad Sci U S A* **85**, 5849-5853, doi:10.1073/pnas.85.16.5849 (1988).

47 Wu, S. Y., Lee, A. Y., Lai, H. T., Zhang, H. & Chiang, C. M. Phospho switch triggers Brd4 chromatin binding and activator recruitment for gene-specific targeting. *Mol Cell* **49**, 843-857, doi:10.1016/j.molcel.2012.12.006 (2013).

48 Wang, R., Yang, J. F., Ho, F., Robertson, E. S. & You, J. Bromodomain-Containing Protein BRD4 Is Hyperphosphorylated in Mitosis. *Cancers (Basel)* **12**, doi:10.3390/cancers12061637 (2020).

49 Demine, S., Renard, P. & Arnould, T. Mitochondrial Uncoupling: A Key Controller of Biological Processes in Physiology and Diseases. *Cells* **8**, doi:10.3390/cells8080795 (2019).

50 Raux, B. *et al.* Exploring Selective Inhibition of the First Bromodomain of the Human Bromodomain and Extra-terminal Domain (BET) Proteins. *J Med Chem* **59**, 1634-1641, doi:10.1021/acs.jmedchem.5b01708 (2016).

51 Noguchi-Yachide, T., Sakai, T., Hashimoto, Y. & Yamaguchi, T. Discovery and structure-activity relationship studies of N6-benzoyladenine derivatives as novel BRD4 inhibitors. *Bioorg Med Chem* **23**, 953-959, doi:10.1016/j.bmc.2015.01.022 (2015).

52 Picaud, S. *et al.* 9H-purine scaffold reveals induced-fit pocket plasticity of the BRD9 bromodomain. *J Med Chem* **58**, 2718-2736, doi:10.1021/jm501893k (2015).

53 Pawar, A., Gollavilli, P. N., Wang, S. & Asangani, I. A. Resistance to BET Inhibitor Leads to Alternative Therapeutic Vulnerabilities in Castration-Resistant Prostate Cancer. *Cell Rep* **22**, 2236-2245, doi:10.1016/j.celrep.2018.02.011 (2018).

54 Rathert, P. *et al.* Transcriptional plasticity promotes primary and acquired resistance to BET inhibition. *Nature* **525**, 543-547, doi:10.1038/nature14898 (2015).

55 Cross, B. C. *et al.* Increasing the performance of pooled CRISPR-Cas9 drop-out screening. *Sci Rep* **6**, 31782, doi:10.1038/srep31782 (2016).

56 Montague, T. G., Cruz, J. M., Gagnon, J. A., Church, G. M. & Valen, E. CHOPCHOP: a CRISPR/Cas9 and TALEN web tool for genome editing. *Nucleic Acids Res* **42**, W401-407, doi:10.1093/nar/gku410 (2014).

57 Bigenzahn, J. W. *et al.* LZTR1 is a regulator of RAS ubiquitination and signaling. *Science* **362**, 1171-1177, doi:10.1126/science.aap8210 (2018).

58 Love, M. I., Huber, W. & Anders, S. Moderated estimation of fold change and dispersion for RNA-seq data with DESeq2. *Genome Biol* **15**, 550, doi:10.1186/s13059-014-0550-8 (2014).

59 Sergushichev, A. A. An algorithm for fast preranked gene set enrichment analysis using cumulative statistic calculation. *bioRxiv*, doi:10.1101/060012 (2016).

60 Kamentsky, L. *et al.* Improved structure, function and compatibility for CellProfiler: modular high-throughput image analysis software. *Bioinformatics* **27**, 1179-1180, doi:10.1093/bioinformatics/btr095 (2011).

61 Schick, S. *et al.* Systematic characterization of BAF mutations provides insights into intracomplex synthetic lethalities in human cancers. *Nat Genet* **51**, 1399-1410, doi:10.1038/s41588-019-0477-9 (2019).

62 Jiang, H., Lei, R., Ding, S. W. & Zhu, S. Skewer: a fast and accurate adapter trimmer for next-generation sequencing paired-end reads. *BMC Bioinformatics* **15**, 182, doi:10.1186/1471-2105-15-182 (2014).

63 Langmead, B. & Salzberg, S. L. Fast gapped-read alignment with Bowtie 2. *Nat Methods* **9**, 357-359, doi:10.1038/nmeth.1923 (2012).

64 Zhang, Y. *et al.* Model-based analysis of ChIP-Seq (MACS). *Genome Biol* **9**, R137, doi:10.1186/gb-2008-9-9-r137 (2008).

65 Ramirez, F. *et al.* deepTools2: a next generation web server for deep-sequencing data analysis. *Nucleic Acids Res* **44**, W160-165, doi:10.1093/nar/gkw257 (2016).

Extended Data Fig. 1. Characterization and validation of BRD4 reporter REDS clones. a, RFP expression in REDS1, REDS15 and REDS17 clones with DMSO or 1 μM (+)-JQ1 treatment for 72 h. b, Representation of RFP insertion gene locus in REDS15 and REDS17 clones. Single RFP was inserted in chromosome 12, 410 bp (REDS15) or 673 bp (REDS17) upstream of STX2.

Extended Data Fig. 2. Generation of SLC nucleoside transporters knockout. To generate the SLC knockout cells, we co-infected REDS cells with lentivirus-based Cas9-sgRNA expression cassettes (pLentiCRISPRv3-PuromycinR), pLentiGuide-BlasticidinR and pLentiGuide-NeomycinR carrying sgRen or sgSLC. The control and knockout cells were selected with 0.5 μg/ml puromycin, 20 μg/ml blasticidin and 250 μg/ml neomycin for 7 days.

Extended Data Fig. 3. Purine supplementation attenuates BRD4 inhibition phenotype in exogenous nucleosides limited condition. a, Relative RFP intensity in REDS1 and REDS15 clones cultured in medium supplemented with 10% dialyzed serum (dFBS) over time. The log2 fold change of the RFP intensity was normalized with cells cultured in medium supplemented with 10% FBS. Mean ± s.d., n = 3 biologically independent samples. The p-value was calculated by unpaired t-tests. b, Relative RFP intensity in REDS15 cells after growing in medium supplemented with 10% dFBS for 10 days and further exogenously added with purine (adenosine and guanosine) or pyrimidine nucleosides (cytidine and thymidine) for 72 h. Mean ± s.d., n = 3 biologically independent samples.

Extended Data Fig. 4. Identification of the metabolic pathway involving in BRD4 regulation. a, Summary of the targeted pathways of metabolic compound library. b, Representative images of REDS15 cells with DMSO, 1 μM (+)-JQ1, 10 μM CPI-0610 or 10 μM 6-MP treatment for 72 h. Scale bar, 100 μm. c, RFP expression in REDS1 cells with indicated concentrations of 6-MP-related compounds treatment for 72 h. d, RFP expression in REDS1 and REDS15 cells with indicated concentrations of pelitrexol and lometrexol treatment for 72 h. e, RFP expression in REDS1 and REDS15 cells with indicated concentrations of pyrimidine metabolism inhibitors treatment for 72 h. f, Scheme of purine metabolism, enzymes participating in the cascade and the pathway intermediates.

Extended Data Fig. 5. Investigation of BRD4 and its related histone acetylation markers expression in REDS15 cells upon purine metabolism impairment. a, Western blot analysis of BRD4 expression in chromatin-bound, nucleoplasm and cytoplasmic fractions after 10 μM pelitrexol or lometrexol treatment for 72 h. Lamin B1, GAPDH and histone H3 were markers for nuclear-chromatin, cytoplasm and chromatin-bound protein fractions. b,c, Western blot analysis of BRD4, H3K27ac and pan-H3ac expression in cells with 10 μM 6-MP treatment or bearing triple SLC knockout (SLC TKO, 12 days after sgRNA transduction) (b), and in cells with 10 μM pelitrexol or lometrexol treatment for 72 h (c). ns, non-specific band.

Extended Data Fig. 6. BRD4 ChIP-seq in REDS15 cells upon purine metabolism impairment. a, Principal component analysis on BRD4 ChIP-seq raw counts in cells with indicated treatments. Upper panel, with 3 replicates of individual treatment. Lower panel, with replicate number 3 in 6-MP treated group (6-MP_BRD4_IP_rep3) excluded. b, Heatmaps representing BRD4 binding enrichment for all ChIP-seq consensus peak regions (N = 24,140) in individual replicates. c, Aggregate coverage plots showing mean enrichment for the different ChIP-seq consensus peak regions in cells with 10 μM 6-MP or 1 μM (+)-JQ1 treatment or bearing triple SLC knockout (SLC TKO), with ±10 kb centred on the regions. d, Genome browser visualization of BRD4 binding at its representative target genes MYC and BCL-2 in cells with indicated treatments.

Extended Data Fig. 7. Transcriptome analysis in cells with purine metabolism impairment. a,b, Heat map of relative transcriptional change (a) and Pearson correlation coefficient of gene expression (b) in REDS1 and REDS15 clones with triple SLC knockout (SLC TKO, 12 days after sgRNA transduction), 10 μM 6-MP or 1 μM (+)-JQ1 treatment for 72 h. The log2 fold change of gene expression was calculated relatively to sgRen or DMSO treated cells. c,d, GSEA of the downregulated genes from the merged RNA-seq results of REDS1 and REDS15 clones (c). The GSEA plots show downregulation of MYC and E2F target gene sets (d). e, RT–qPCR analysis of MYC expression by using two different MYC primer sets in REDS1, REDS15 and K562 cells. Mean ± s.d., n = 3 biologically independent samples. f, Heat map of relative transcriptional change of purine metabolism genes in REDS1 and REDS15 clones with 10 μM 6-MP or 1 μM (+)-JQ1 treatment for 72 h or with triple SLC knockout (SLC TKO, 12 days after sgRNA transduction).

Extended Data Fig. 8. Loss of BRD4 inhibition phenotype in REDS15 cells after SLC sgRNA transduction for 23 days. a, RFP expression in cells with SLC knockout 23 days after sgRNA transduction. b, TIDE analysis of SLC sgRNA editing efficiency. c, Metabolite composition in cells with triple SLC knockout (SLC TKO) 23 days after sgRNA transduction. The log2 fold change of metabolites level was calculated relatively to sgRen cells. AA, amino acids; NT, nucleotides; NB, nucleobases; NS, nucleosides. d, Western blot analysis of BRD4 expression in chromatin-bound, nucleoplasm and cytoplasmic fractions. Lamin B1, GAPDH and histone H3 were markers for nuclear-chromatin, cytoplasm and chromatin-bound protein fractions. ns, non-specific band. e, The viability of triple SLC knockout (SLC TKO) day 12 and day 23 cells after lometrexol treatment for 72 h. Cell numbers were measured by CASY Cell Counter and Analyzer and normalized with the control sgRen day 12 or day 23 cells. Mean ± s.d., n = 3 biologically independent samples. f, Relative RFP intensity in sgRen or triple SLC knockout (SLC TKO) day 12 or 23 cells with lometrexol treatment for 72 h. The log2 fold change of the RFP intensity was normalized with sgRen cells with DMSO treatment. g, Heat map of the relative transcriptional change of genes in SLC28, SLC29 and SLC35 families in REDS15 triple SLC knockout day 12 and day 23 cells normalized with the respective controls sgRen day 12 and day 23 cells. h, Stable isotope labeled +1 adenine or +3 glycine tracing into nucleotides in sgRen or triple SLC knockout (SLC TKO) day 12 and day 23 cells. Mean ± s.d., n = 3 biologically independent samples. The p-value was calculated by unpaired t-tests.

Extended Data Fig. 9. Inhibition of nucleoside transport or de novo purine synthesis synergistically impairs leukemia cells growth with CPI-0610. a,b, Dose-response matrix displaying the cell viability measured using CellTiter Glo (a) and CASY Cell Counter and Analyzer (b) of Jurkat E6.1, Raji and K562 cells treated with indicated concentrations of CPI-0610 or 6-MP, or in combination for 72 h.

Extended Data Fig. 10. Investigating the rescuing effect of nucleotide metabolites on BRD4 functionality. a-c, Relative RFP expression in REDS1 and REDS15 cells co-treated with 100 μM nucleotide metabolites and 10 μM SLC29A4 inhibitor TC-T 6000 for 72 h (a), 10 nM dBET6 for 24 h (b) and 1 μM (+)-JQ1 for 72 h (c). The log2 fold change was normalized with DMSO treated cells. d, Western blot analysis of BRD4, c-MYC and BRD4-related histone acetylation markers expression in REDS15 cells co-treated with 100 μM nucleotide metabolites and 10 μM 6-MP or 1 μM (+)-JQ1 for 72 h. ns, non-specific band.

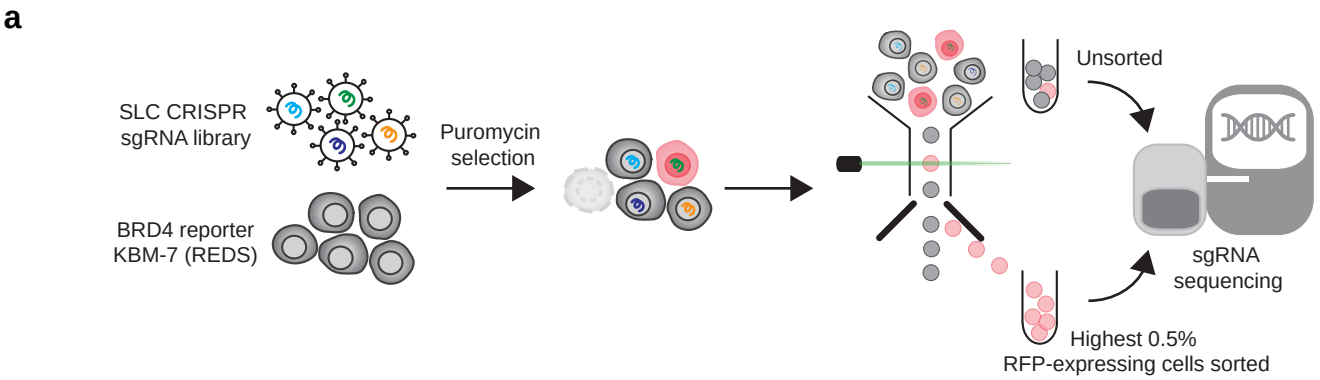
a
SLC CRISPR
sgRNA library
BRD4 reporter
KBM-7 (REDS)
Puromycin
selection
Unsorted
sgRNA
sequencing
Highest 0.5%
RFP-expressing cells sorted

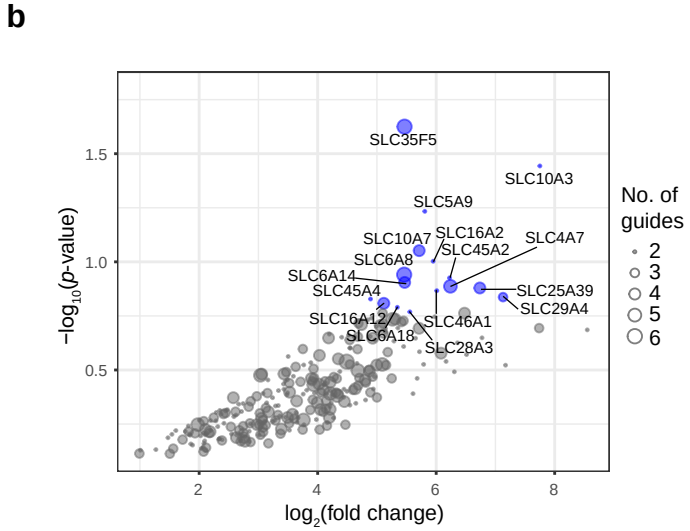
b
SLC35F5
SLC10A3
SLC5A9
SLC10A7
SLC16A2
SLC45A2
SLC4A7
SLC6A8
SLC6A14
SLC45A4
SLC25A39
SLC29A4
SLC16A12
SLC46A1
SLC6A18
SLC28A3
No. of
guides
2
3
4
5
6
−log10(p-value)
log2(fold change)

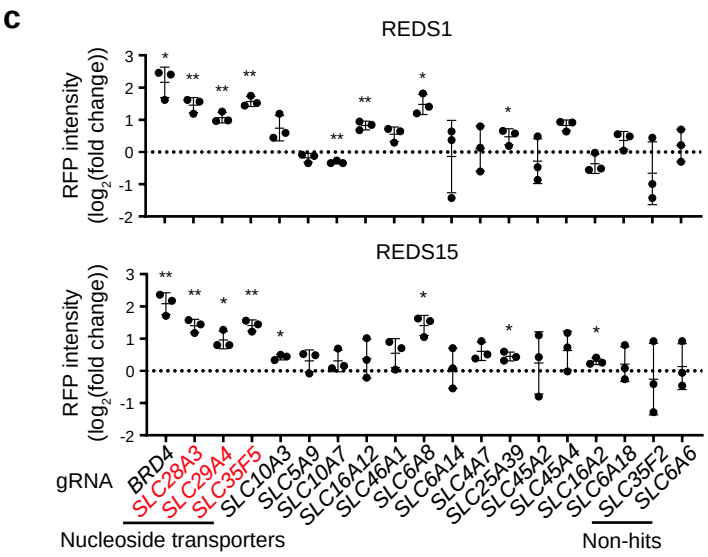
c
REDS1
REDS15
RFP intensity
(log2(fold change))
gRNA
BRD4
SLC28A3
SLC29A4
SLC35F5
SLC10A3
SLC5A9
SLC10A7
SLC16A12
SLC46A1
SLC6A8
SLC6A14
SLC4A7
SLC25A39
SLC45A2
SLC45A4
SLC16A2
SLC6A18
SLC35F2
SLC6A6
Nucleoside transporters
Non-hits

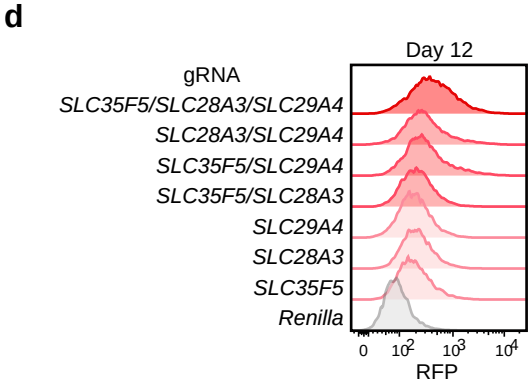
d
Day 12
gRNA
SLC35F5/SLC28A3/SLC29A4
SLC28A3/SLC29A4
SLC35F5/SLC29A4
SLC35F5/SLC28A3
SLC29A4
SLC28A3
SLC35F5
Renilla
RFP

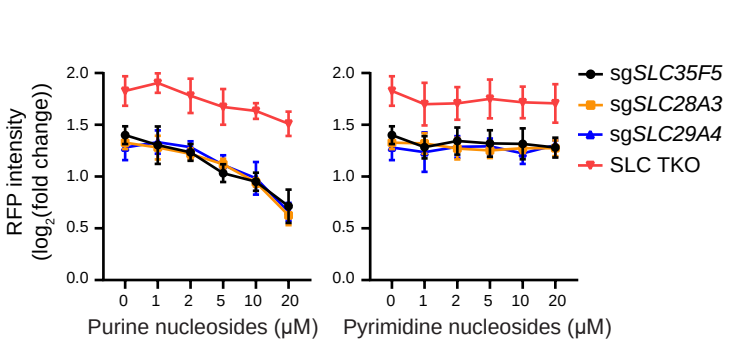
e
RFP intensity
(log2(fold change))
sgSLC35F5
sgSLC28A3
sgSLC29A4
SLC TKO
Purine nucleosides (μM)
Pyrimidine nucleosides (μM)

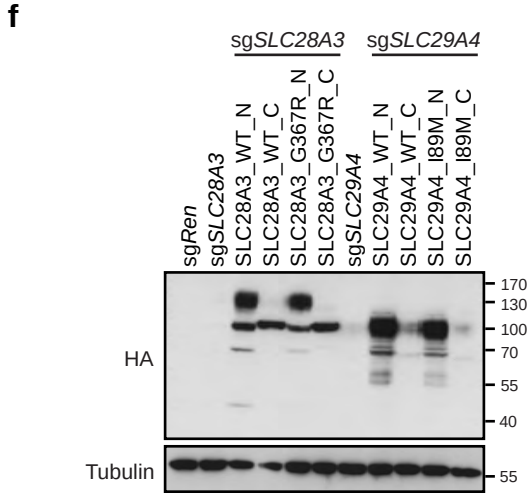
f
sgSLC28A3
sgSLC29A4
sgRen
sgSLC28A3
SLC28A3_WT_N
SLC28A3_WT_C
SLC28A3_G367R_N
SLC28A3_G367R_C
sgSLC29A4
SLC29A4_WT_N
SLC29A4_WT_C
SLC29A4_I89M_N
SLC29A4_I89M_C
HA
Tubulin
170
130
100
70
55
40
55

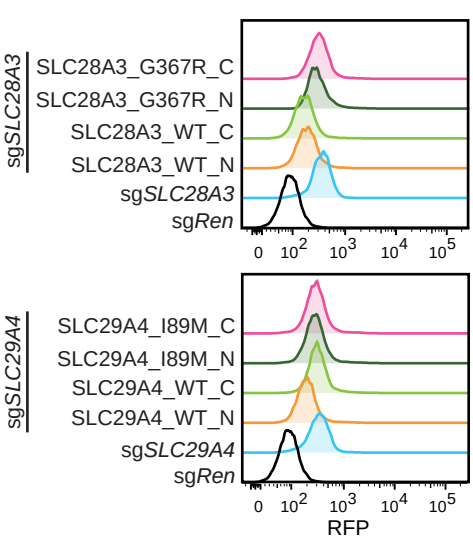
g
sgSLC28A3
SLC28A3_G367R_C
SLC28A3_G367R_N
SLC28A3_WT_C
SLC28A3_WT_N
sgSLC28A3
sgRen
sgSLC29A4
SLC29A4_I89M_C
SLC29A4_I89M_N
SLC29A4_WT_C
SLC29A4_WT_N
sgSLC29A4
sgRen
RFP

Figure 1

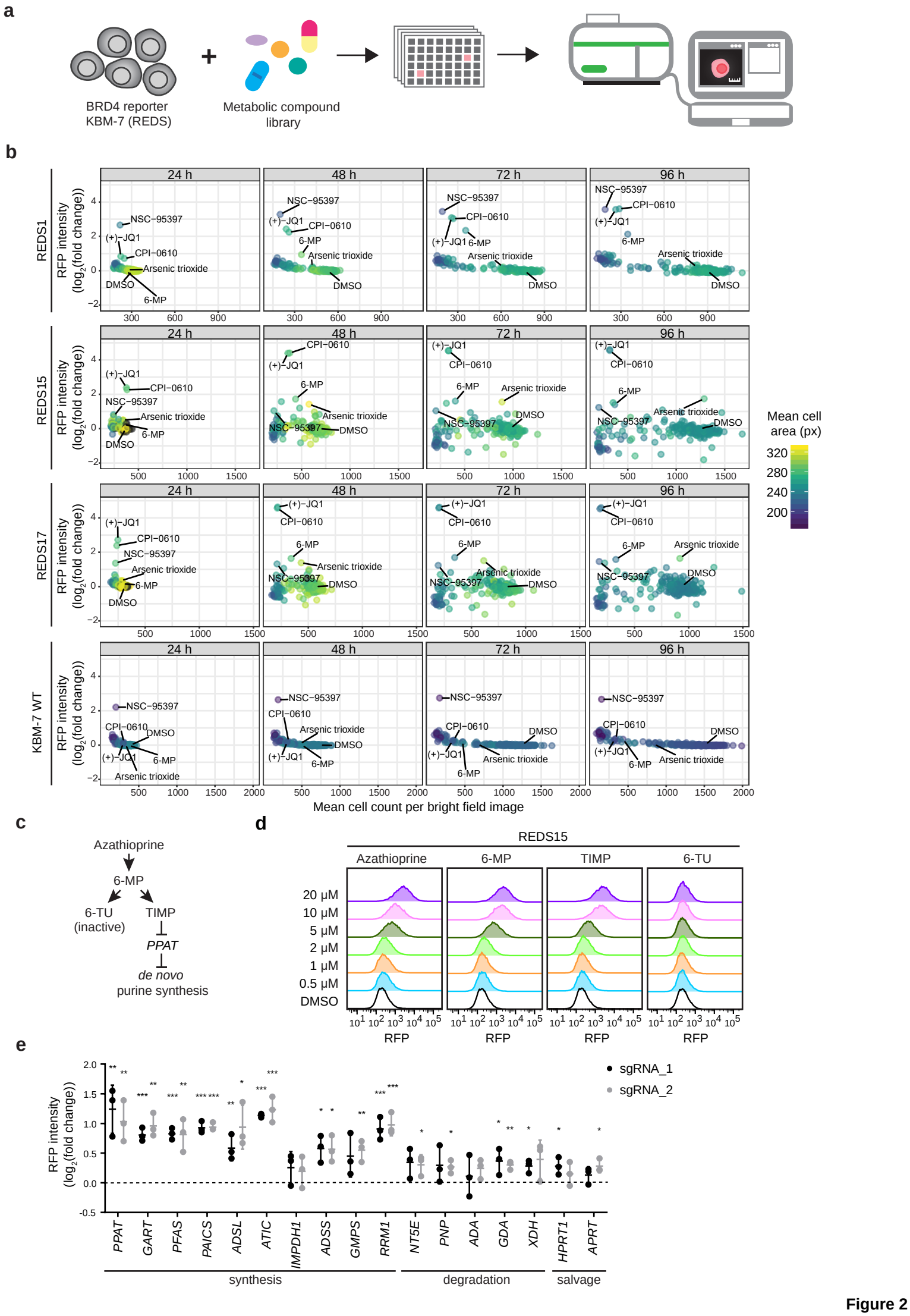
a
BRD4 reporter
KBM-7 (REDS)
Metabolic compound
library
b
REDS1
REDS15
REDS17
KBM-7 WT
24 h
48 h
72 h
96 h
RFP intensity
(log2(fold change))
Mean cell count per bright field image
Mean cell
area (px)
320
280
240
200
NSC−95397
(+)−JQ1
CPI−0610
6-MP
Arsenic trioxide
DMSO
c
Azathioprine
6-MP
6-TU
(inactive)
TIMP
PPAT
de novo
purine synthesis
d
REDS15
Azathioprine
6-MP
TIMP
6-TU
20 μM
10 μM
5 μM
2 μM
1 μM
0.5 μM
DMSO
RFP
e
RFP intensity
(log2(fold change))
sgRNA_1
sgRNA_2
PPAT
GART
PFAS
PAICS
ADSL
ATIC
IMPDH1
ADSS
GMPS
RRM1
NT5E
PNP
ADA
GDA
XDH
HPRT1
APRT
synthesis
degradation
salvage

Figure 2

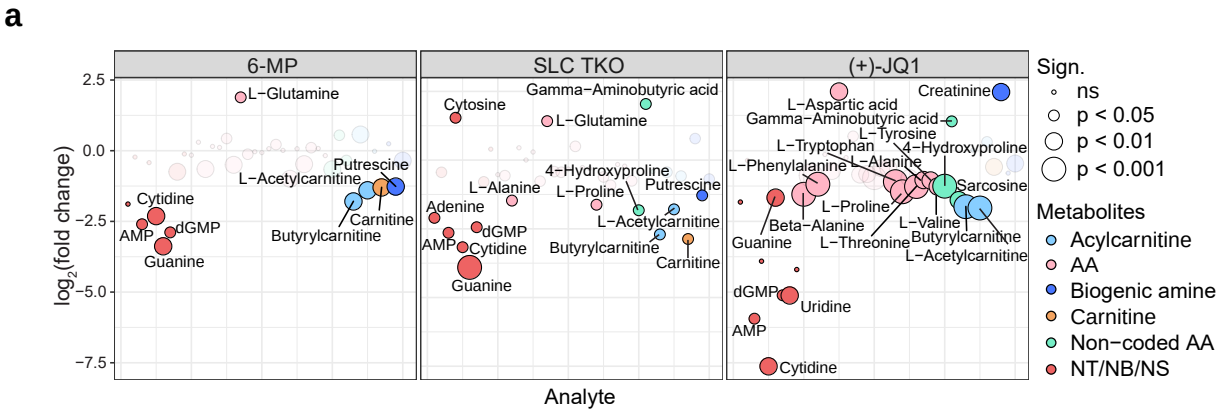
a
6-MP
SLC TKO
(+)-JQ1
log2(fold change)
Analyte
L−Glutamine
Putrescine
L−Acetylcarnitine
Cytidine
dGMP
AMP
Carnitine
Butyrylcarnitine
Guanine
Cytosine
Gamma−Aminobutyric acid
4−Hydroxyproline
L−Alanine
L−Proline
Adenine
Creatinine
L−Aspartic acid
L−Tyrosine
L−Tryptophan
L−Phenylalanine
Sarcosine
Beta−Alanine
L−Valine
L−Threonine
dGMP
Uridine
Sign.
ns
p < 0.05
p < 0.01
p < 0.001
Metabolites
Acylcarnitine
AA
Biogenic amine
Carnitine
Non−coded AA
NT/NB/NS

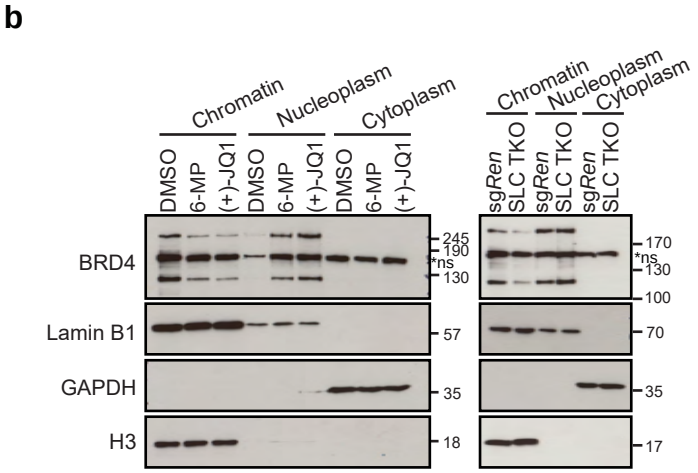
b
Chromatin
Nucleoplasm
Cytoplasm
DMSO
6-MP
(+)-JQ1
sgRen
SLC TKO
BRD4
Lamin B1
GAPDH
H3
245
190
130
100
70
57
35
18
17
170
*ns

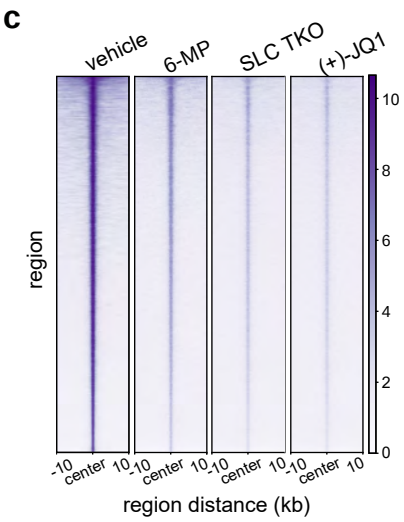
c
vehicle
6-MP
SLC TKO
(+)-JQ1
region
region distance (kb)
-10
center
10

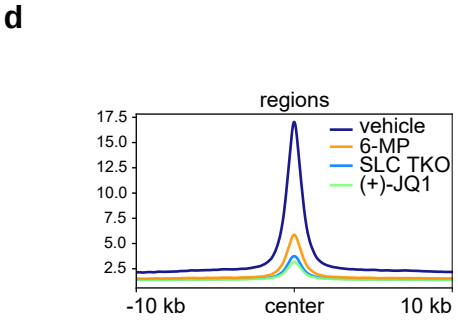
d
regions
vehicle
6-MP
SLC TKO
(+)-JQ1
-10 kb
center
10 kb

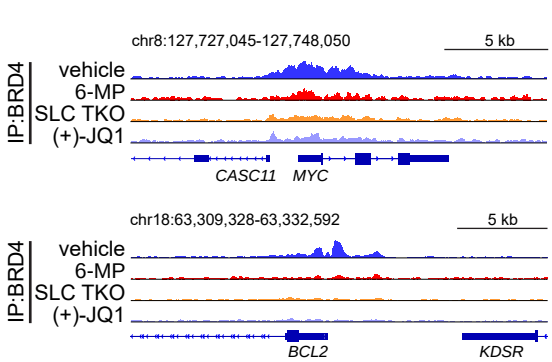
e
chr8:127,727,045-127,748,050
5 kb
IP:BRD4
vehicle
6-MP
SLC TKO
(+)-JQ1
CASC11
MYC
chr18:63,309,328-63,332,592
BCL2
KDSR

Figure 3

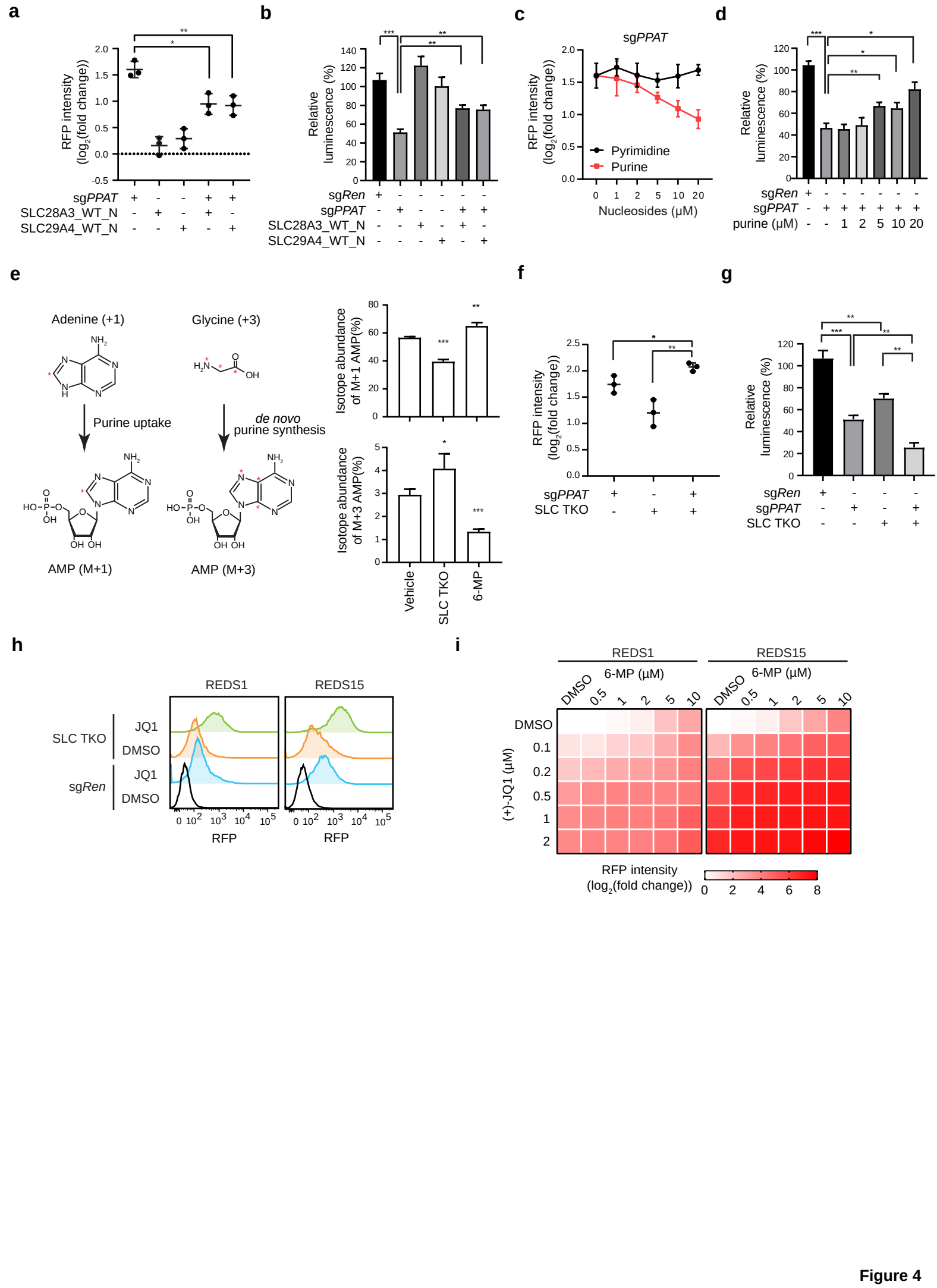
a
RFP intensity (log2(fold change))
sgPPAT
SLC28A3_WT_N
SLC29A4_WT_N
b
Relative luminescence (%)
sgRen
sgPPAT
SLC28A3_WT_N
SLC29A4_WT_N
c
sgPPAT
RFP intensity (log2(fold change))
Pyrimidine
Purine
Nucleosides (μM)
d
Relative luminescence (%)
sgRen
sgPPAT
purine (μM)
e
Adenine (+1)
Glycine (+3)
Purine uptake
de novo purine synthesis
AMP (M+1)
AMP (M+3)
Isotope abundance of M+1 AMP(%)
Isotope abundance of M+3 AMP(%)
Vehicle
SLC TKO
6-MP
f
RFP intensity (log2(fold change))
sgPPAT
SLC TKO
g
Relative luminescence (%)
sgRen
sgPPAT
SLC TKO
h
REDS1
REDS15
SLC TKO
JQ1
DMSO
sgRen
JQ1
DMSO
RFP
RFP
i
REDS1
REDS15
6-MP (μM)
DMSO
0.5
1
2
5
10
(+)-JQ1 (μM)
DMSO
0.1
0.2
0.5
1
2
RFP intensity (log2(fold change))
0
2
4
6
8

Figure 4

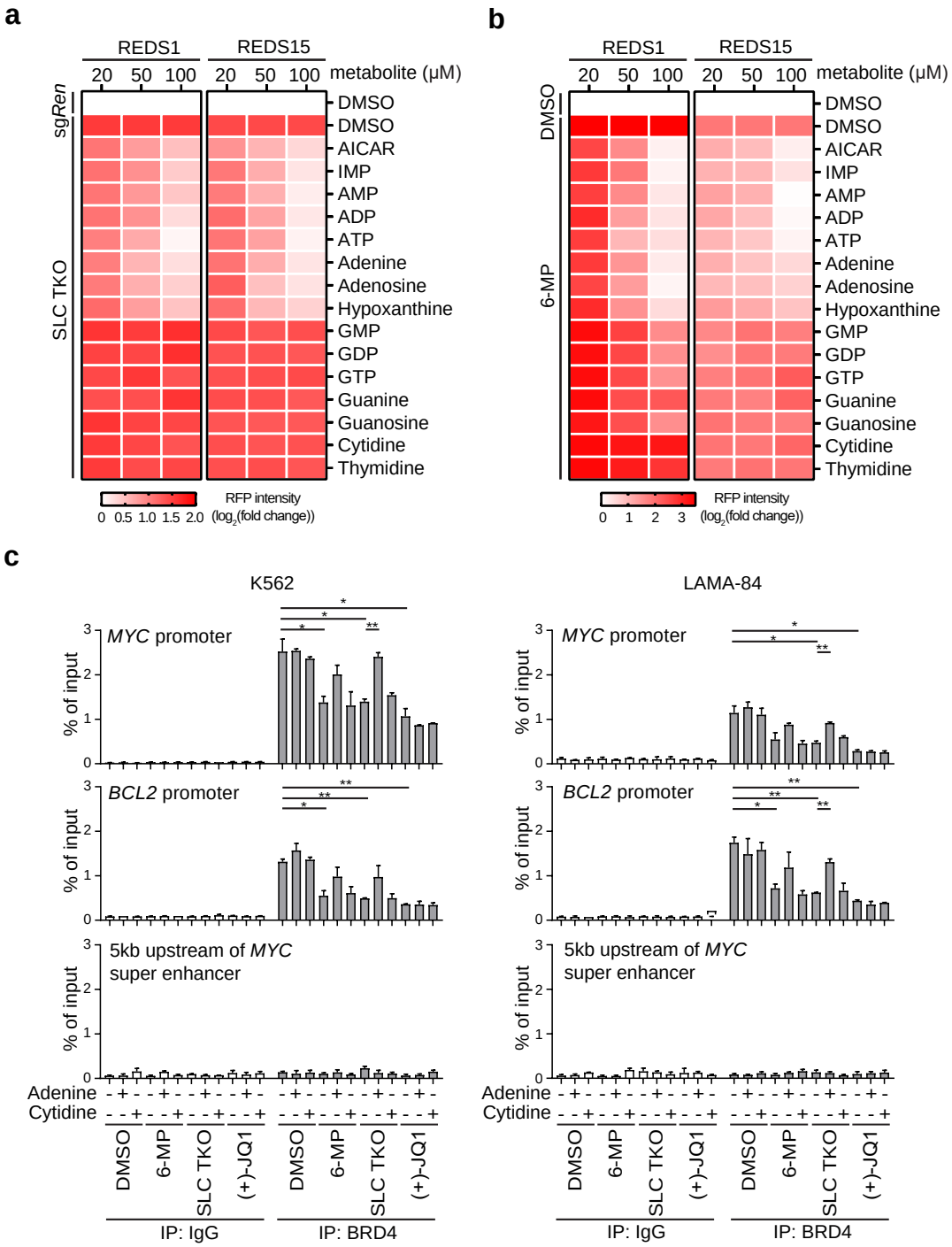
a
REDS1
REDS15
20 50 100 20 50 100 metabolite (μM)
sgRen
SLC TKO
DMSO
DMSO
AICAR
IMP
AMP
ADP
ATP
Adenine
Adenosine
Hypoxanthine
GMP
GDP
GTP
Guanine
Guanosine
Cytidine
Thymidine
RFP intensity
0 0.5 1.0 1.5 2.0 (log2(fold change))
b
REDS1
REDS15
20 50 100 20 50 100 metabolite (μM)
DMSO
6-MP
DMSO
DMSO
AICAR
IMP
AMP
ADP
ATP
Adenine
Adenosine
Hypoxanthine
GMP
GDP
GTP
Guanine
Guanosine
Cytidine
Thymidine
RFP intensity
0 1 2 3 (log2(fold change))
c
K562
LAMA-84
MYC promoter
BCL2 promoter
5kb upstream of MYC super enhancer
% of input
Adenine
Cytidine
DMSO
6-MP
SLC TKO
(+)-JQ1
IP: IgG
IP: BRD4
d
BRD4 ON
BRD4 OFF
Purine/adenine
Nucleoside transporter (SLC)
Purine uptake
de novo purine synthesis
BRD4
MYC target genes ON
1. Lack of purine source
2. Lack of purine uptake
3. Inhibition of de novo purine synthesis
de novo purine synthesis
BRD4
MYC target genes OFF

Figure 5

a

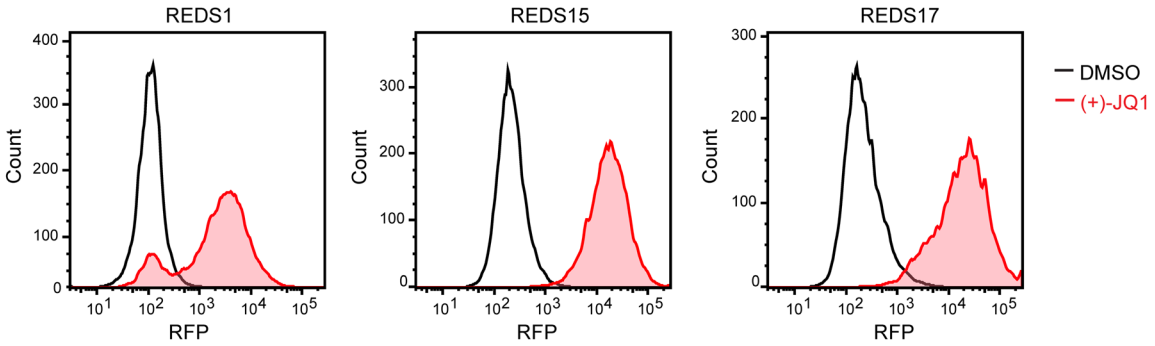

b

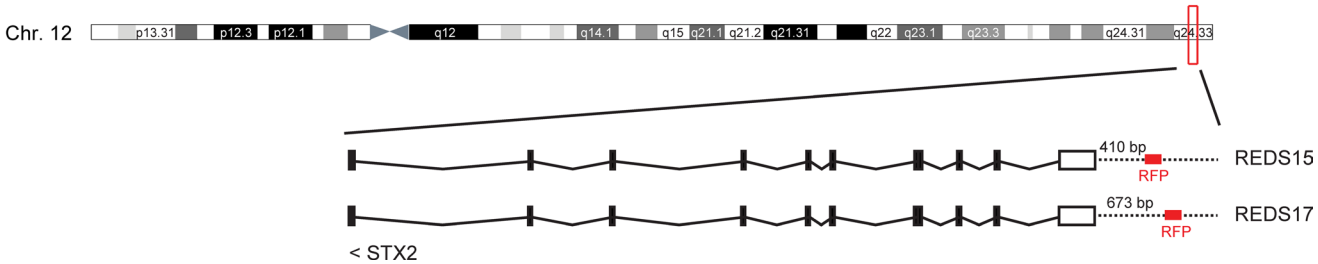

Extended Data Fig. 1

SIngle SLC KO (SKO) generation

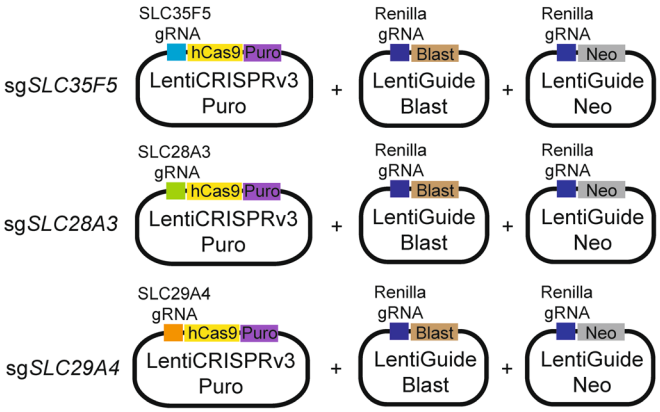

Dual SLC KO (DKO) generation

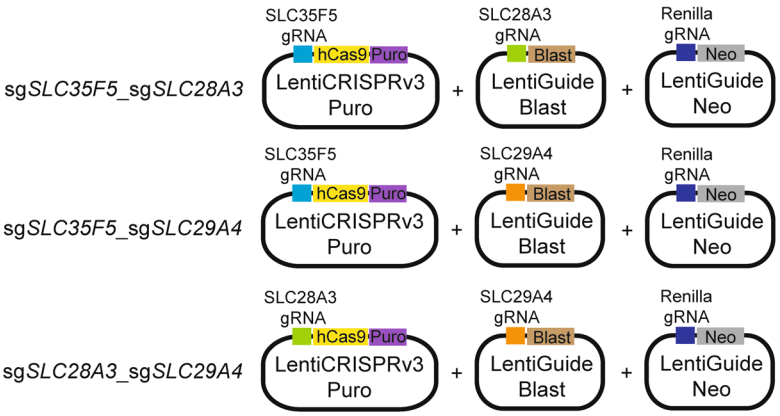

Triple SLC KO (TKO) generation

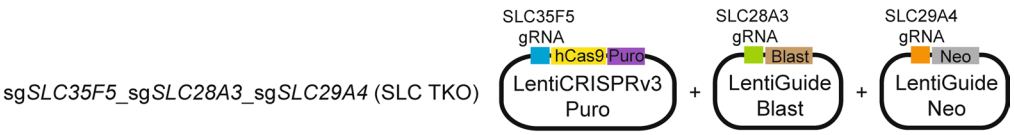

Renilla control

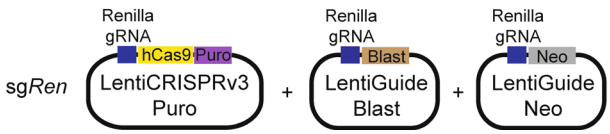

Extended Data Fig. 2

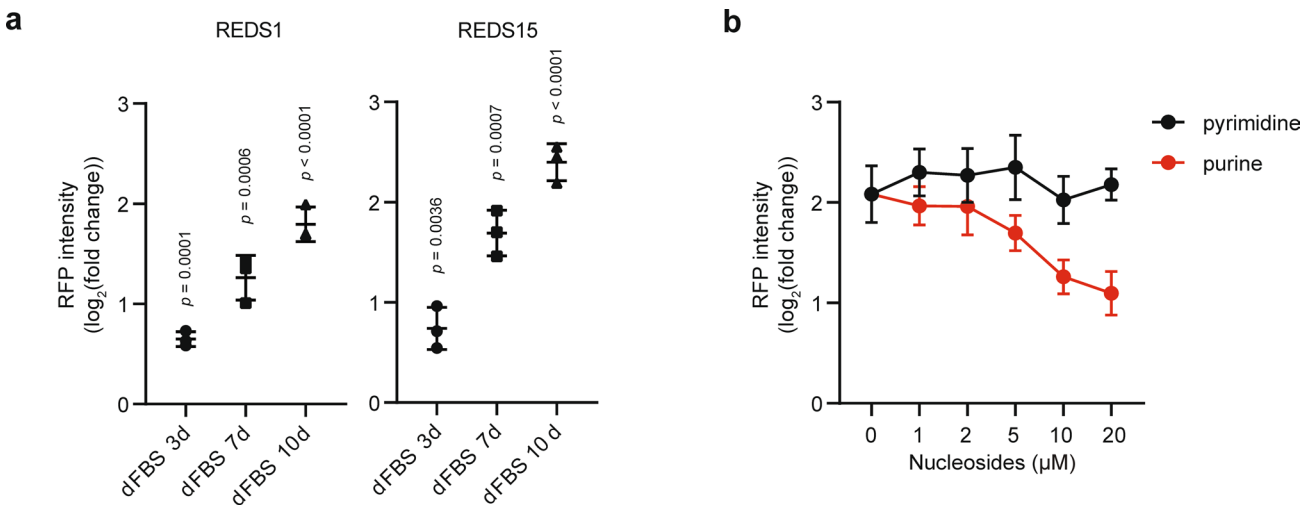

Extended Data Fig. 3

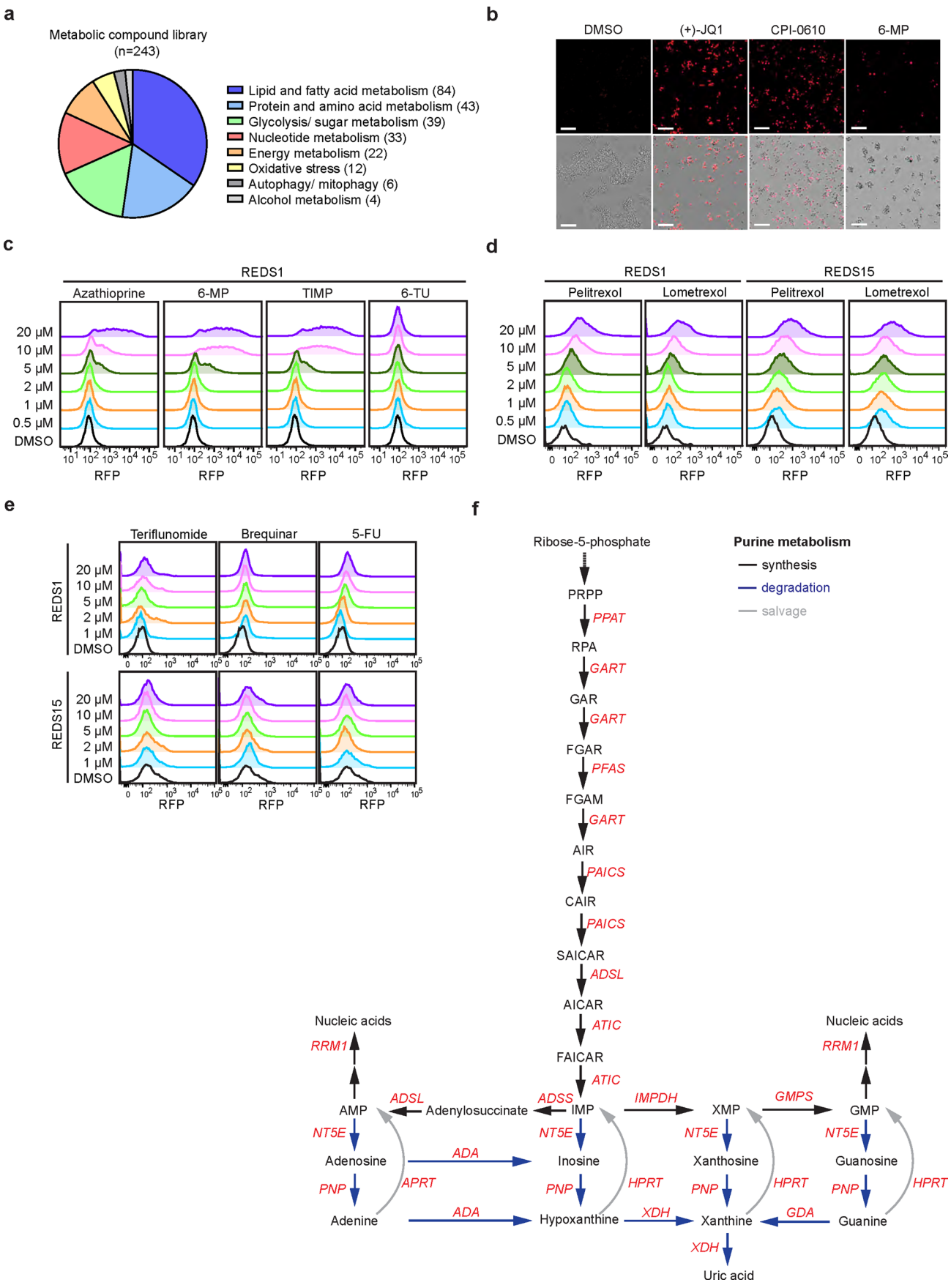

Extended Data Fig. 4

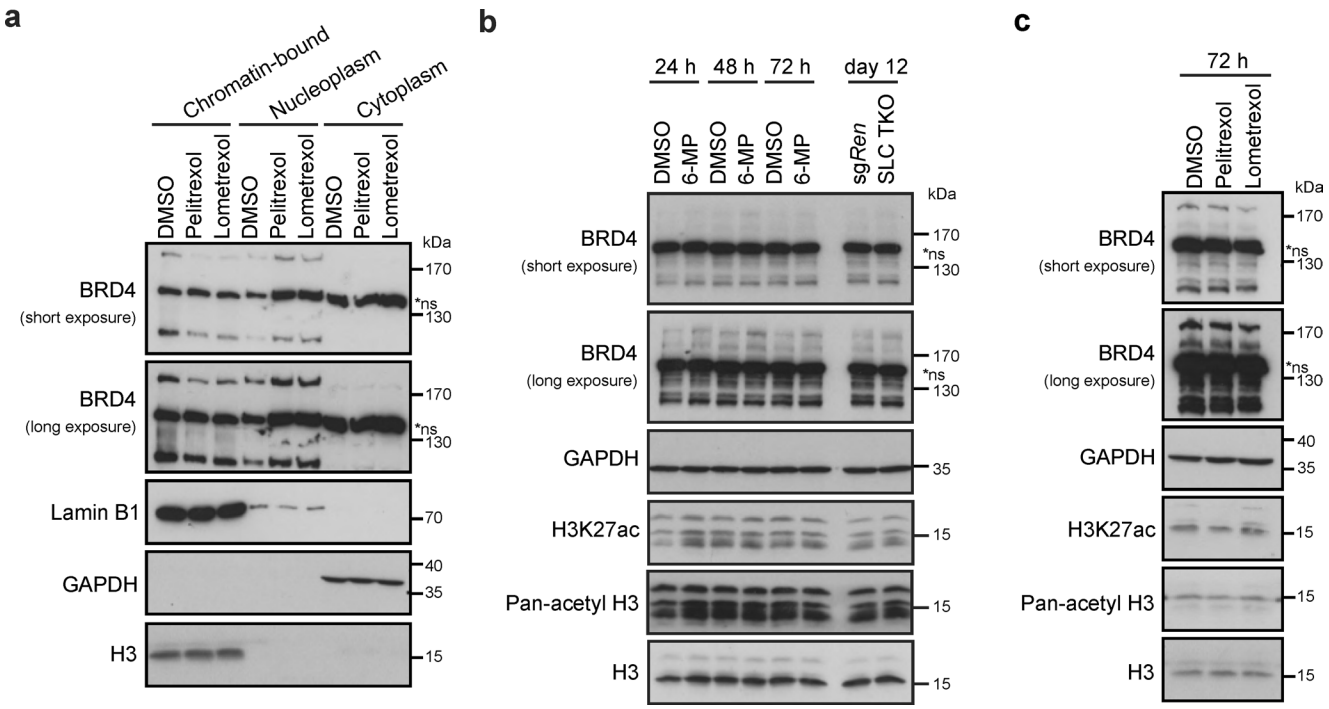

Extended Data Fig. 5

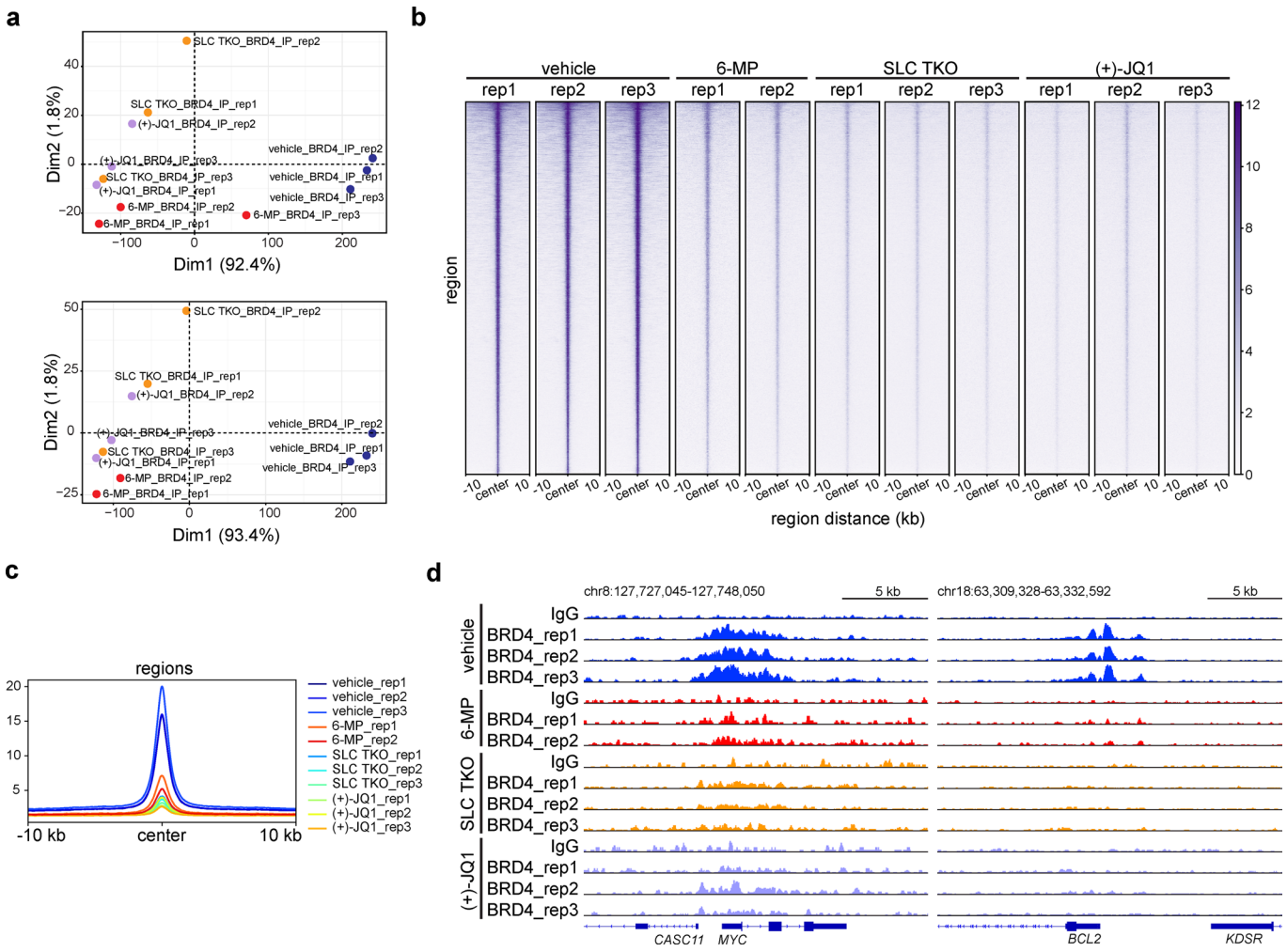

Extended Data Fig. 6

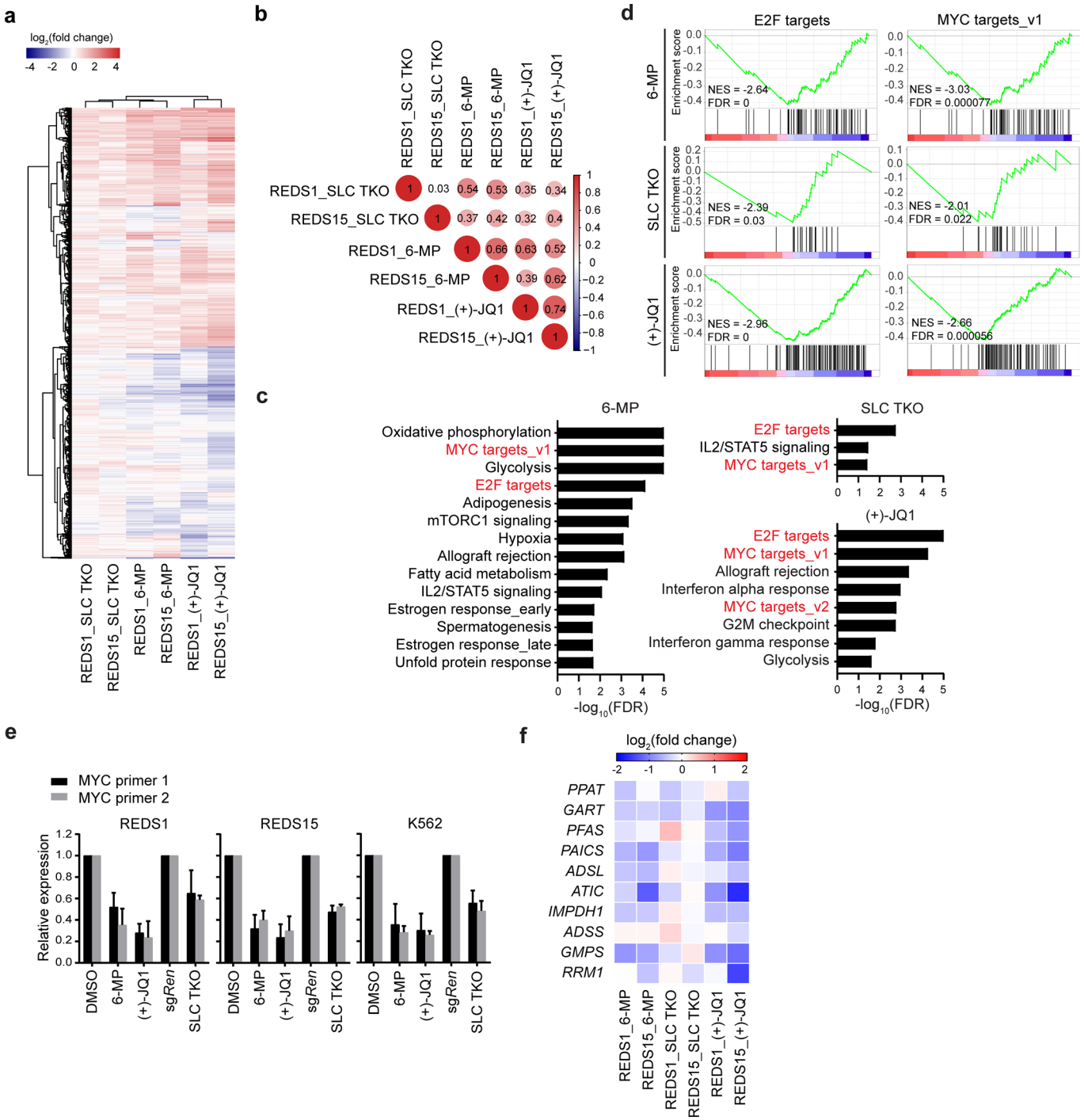

Extended Data Fig. 7

a

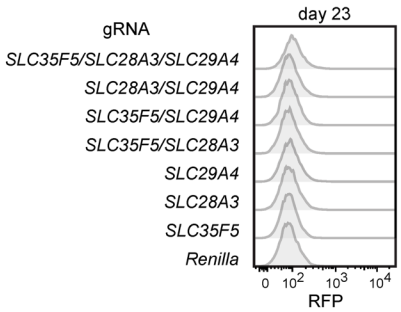

b

	day 12						day 23					
	WT (%)			In-frame deletion(%)			WT (%)			In-frame deletion (%)		
	SLC35F5	*SLC28A3*	*SLC29A4*	*SLC35F5*	*SLC28A3*	*SLC29A4*	*SLC35F5*	*SLC28A3*	*SLC29A4*	*SLC35F5*	*SLC28A3*	*SLC29A4*
SLC TKO	12.8	12.9	15.4	10	9.5	8.1	13.5	11.4	12.7	11.6	10.7	9.6
SLC28A3/SLC29A4		13.7	13.3		9.3	9.2		12.6	12		8.5	10.3
SLC35F5/SLC29A4	10.1		12.4	9.2		8.5	12.3		10.8	9.1		8.8
SLC35F5/SLC28A3	13.4	11.6		10.5	8.8		12.6	12.4		7.8	9.2	
SLC29A4			9.8			8.6			11.5			9.4
SLC28A3		14.7			6.7			12.8			7.9	
SLC35F5	12.3			9.4			14.1			7.5		

c

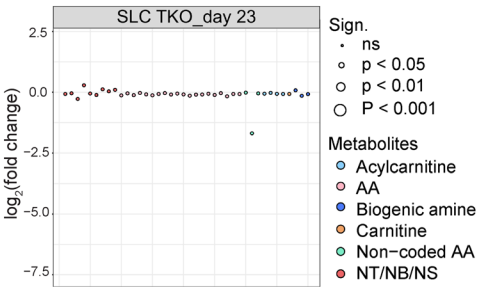

d

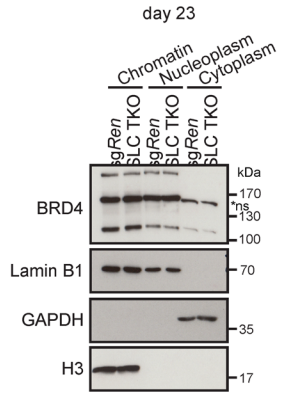

e

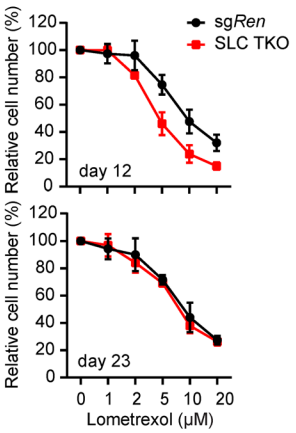

f

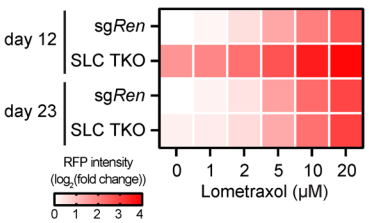

g

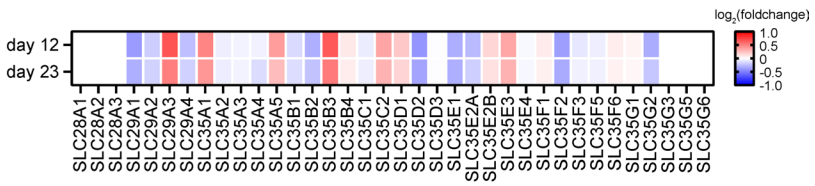

h

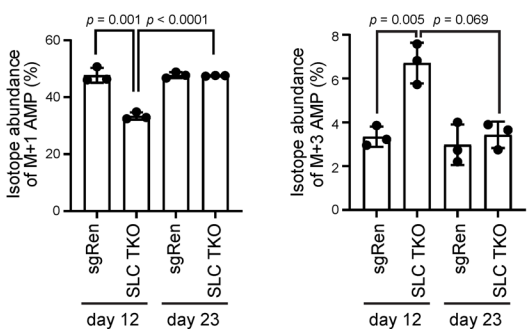

Extended Data Fig. 8

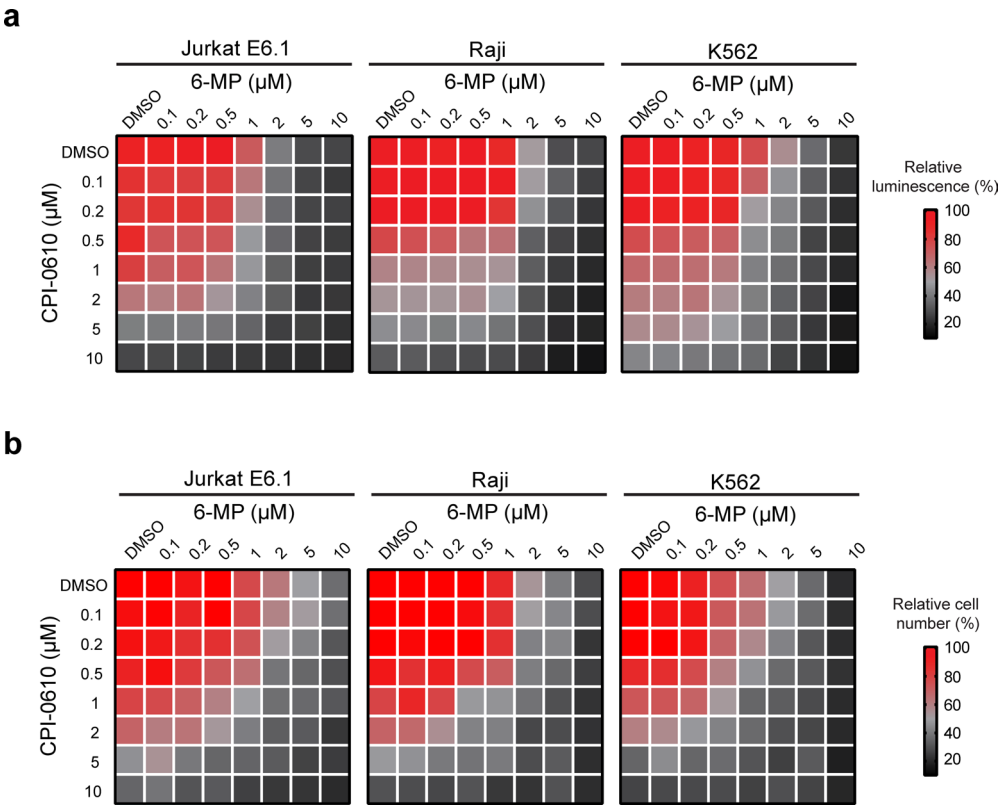

Extended Data Fig. 9

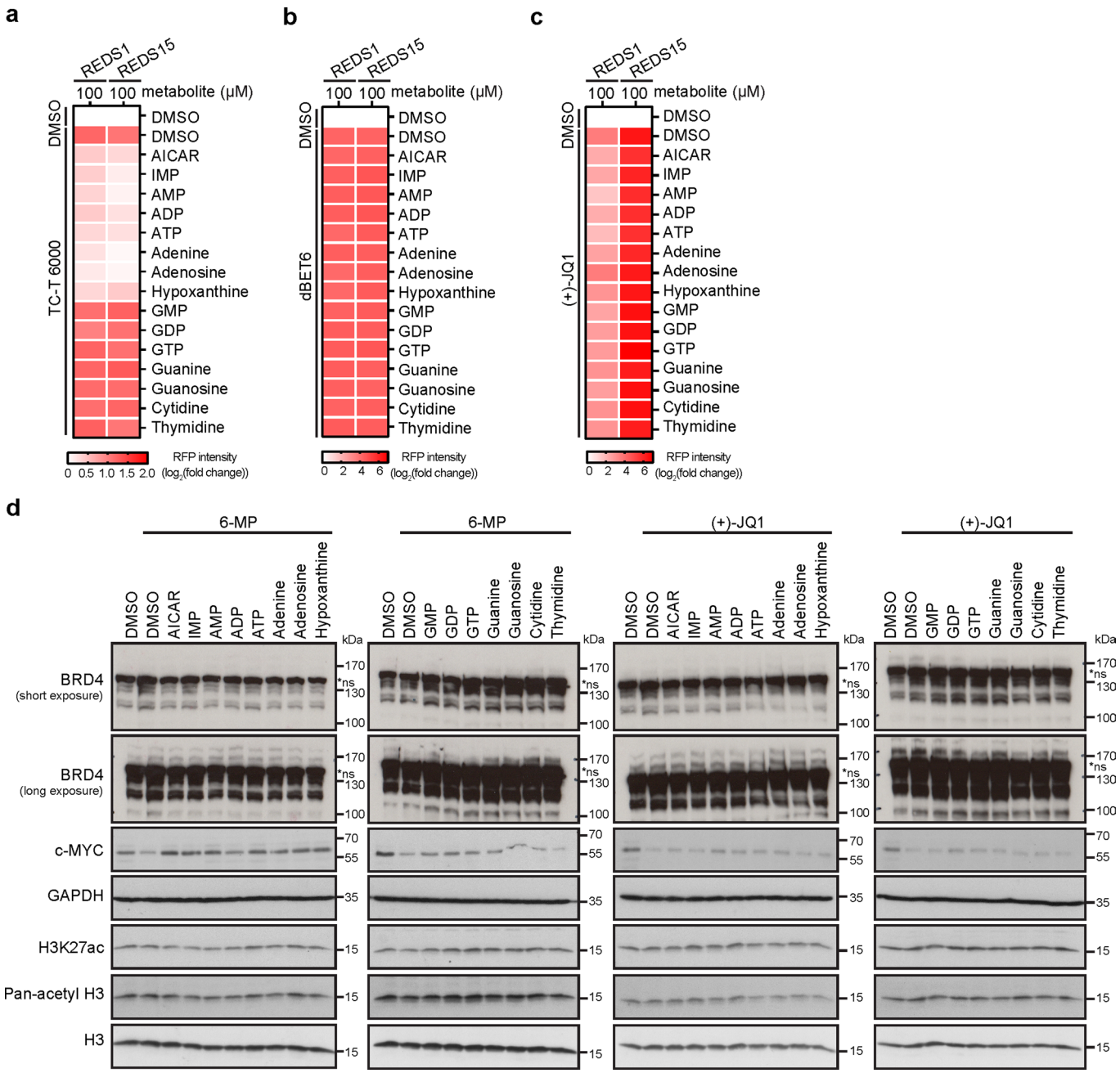

Extended Data Fig. 10